

Transworld Research Network
37/661 (2), Fort P.O., Trivandrum-695 023, Kerala, India



Vibronic Interactions and Electron-Phonon Interactions and Their Role in Modern Chemistry and Physics, 2009: 1-62 ISBN: 978-81-7895-336-6 Editor: Takashi Kato

Electron-phonon coupling in metallic solids from density functional theory

Shyamal K. Bose¹ and Jens Kortus²

¹Department of Physics, Brock University St. Catharines, Ontario L2S 3A1, Canada; ²Institute for Theoretical Physics, TU Bergakademie Freiberg Leipziger Str. 23, D-09599 Freiberg, Germany

Abstract

We present a study of electron-phonon coupling and superconductivity in metallic systems, based on first-principles electronic structure and linear response calculations. Our results are based on the density functional theory and are derived by using the full-potential linear muffin-tin orbitals method. In particular, calculations for phonon spectra, Eliashberg spectral function, and electron-phonon coupling constants are presented. To illustrate the effectiveness of the method, we consider case studies involving some conventional elemental superconductors

Correspondence/Reprint request: Dr. Shyamal K. Bose, Department of Physics, Brock University St. Catharines, Ontario, L2S 3A1, Canada. E-mail: shyamal.bose@brocku.ca

as well as systems that have attracted attention in recent literature. Calculations for boron under pressure, boron-doped systems and boron-based layered superconductors, of which MgB_2 is the most prominent example, are reviewed.

1. Introduction

Electron-phonon (in general, electron-ion) interaction is an important and ubiquitous process in solids, affecting almost all physical properties. In metals, where the relaxation processes depend on both electrons and phonons, all thermodynamic and transport properties are dictated by electron-phonon (EP) interaction, and its effect can be seen in both equilibrium and non-equilibrium properties [1, 2].

The most dramatic manifestation of EP interaction is superconductivity in metals, where all of the properties or processes are drastically modified due to the interaction. As a result, entropy, heat capacity, electrical and thermal conductivities, spin susceptibility, electromagnetic absorption, ultrasonic attenuation and nuclear spin-lattice relaxation of normal and superconducting metals show remarkable differences. The subject of phonon-mediated, or 'conventional', superconductivity has grown rapidly over the years, particularly since the ground-breaking work of Bardeen, Cooper and Schrieffer [3], identifying EP interaction unequivocally as the underlying cause. Excellent reviews of this subject have appeared at various stages of development of the field [2, 4–10]. The present article aims at describing calculations of EP coupling based on *first-principles* electronic structure methods and explores to what extent such calculations, in particular those based on the full-potential linear muffin-tin orbitals (FP-LMTO) method [11–13], have been successful in explaining superconductivity in conventional superconductors.

Superconductivity, discovered by Kamerlingh Onnes [14] in 1911, is a true bulk property of matter representing a macroscopic quantum phenomenon. Parallel to the vanishing of resistivity at and below the superconducting transition temperature T_c , the specific heat Cv changes in a way that is characteristic of a thermodynamic phase transition. The contributions of the electron gas to the specific heat at $T > T_c$ scale linearly with the temperature. At the critical temperature T_c a jump of the specific heat is observed, and at lower temperatures the electronic contributions to Cv decrease exponentially. This exponential decay is a clear sign of the opening of an energy gap in the electronic spectrum, because the electronic part of specific heat is proportional to the density of states at the Fermi level. Further, the Meißner-Ochsenfeld effect [15], the expulsion of magnetic fields from inside of a superconductor, discovered in 1933, also indicates the quantum effect at a macroscopic scale.

Superconductors, therefore, behave as perfect diamagnets, a property which signals potential application as motors or magnetic levitation trains. The behaviour of magnetic fields may be even more complex. Superconductors where the magnetic field is unable to penetrate the material are called type I superconductors. In contrast, in the case of type II superconductors the magnetic field can penetrate in form of flux lines that arrange themselves in a periodic structure called Abrikosov lattice [16]. A type II superconductor in a magnetic field is said to be in a mixed state: in the regions of the flux lines the material is in the normal (nonsuperconducting) state, while outside these regions it is in a superconducting state.

Another notable property is the appearance of a tunneling supercurrent between two superconductors separated by a sufficiently small insulating or normal metal barrier, predicted by Josephson in 1962 [17]. Derived from purely theoretical speculation on symmetry-broken states in superconductors, the Josephson effect is not only real (i.e., observed), but has also found important practical application in very fast switches, highly accurate voltage standards and the measurements of small magnetic fields using SQUID magnetometers - an area of increasing importance in medicine.

The theoretical understanding of superconductivity was lagging behind the experimental discovery by several decades. The Ginzburg-Landau theory of superconductivity, formulated in 1950 [18], was based on phenomenological second-order phase transitions and was able to deliver predictions about critical magnetic fields and currents. However, it failed to offer any insight into the microscopic processes of the mechanism of superconductivity. The long sought-after breakthrough was finally provided by Bardeen, Cooper and Schrieffer (BCS) in 1957 [3]. BCS considered an electron-gas as the model of a metal where the electrons, in addition to being subject to the usual screened Coulomb interaction, interact via exchange of virtual phonons. The character of this second interaction, in its simplest terms, is to be understood as follows: one electron distorts the lattice or creates a phonon, while the second electron responds to the charge imbalance due to the distortion and annihilates the phonon. BCS were able to show that when the total residual interaction is attractive at the Fermi level, the Fermi sea of single electrons becomes unstable against the formation of bound states of paired electrons, known as *Cooper pairs*, and the ground state of these Cooper pairs is energetically favourable to the normal state.

It is important to note that there were several theoretical developments that finally culminated in the BCS theory of superconductivity. As early as 1950, Fröhlich [19] had studied EP interaction in metals using field-theoretical approach. He was able to show that electrons can have an effectively attractive interaction mediated via phonons. Around the same time, or slightly prior to

that, measurements in Hg [20, 21], showing clear dependence of T_c on isotopic mass, the so-called *isotope effect*, were reported, indicating a clear connection between superconductivity and the crystal lattice. In a note added in proof, Fröhlich [19] pointed out that the change in energy of the ground state of the electrons resulting from the EP interaction he had calculated was inversely proportional to the ion mass and thus supported the isotope effect, which had just been observed. Guided by the *isotope effect*, Bardeen [22] considered the interaction of the valence electrons with zero-point vibrations of the lattice and argued that a high density of electrons in a wide energy band and a large interaction between electrons and the lattice are favourable for superconductivity. In the works of both Fröhlich and Bardeen, the ground (superconducting) state involved only single-electron states with energies or self-energies modified by EP interaction, and the idea of paired electron states was still missing. Bardeen and Pines [23] derived an effective electron-electron interaction, including the screened Coulomb interaction and the phonon degrees of freedom. This interaction showed that two electrons can be attracted to each other via exchange of a virtual phonon, if the difference in the electron energies is small compared to the phonon excitation energy. The idea that a superconducting state separated by an energy gap from the first excited state may consist entirely of a non-interacting system of bound electron pairs was put forward by Cooper [24] in 1956, paving the way to the full BCS theory in 1957 [3, 25]. By treating EP interaction via a simplified model BCS were able to explain all the observed properties of a superconductor and put the pairing formalism on a firm footing. The readers can find a more elaborate record of events leading to the BCS theory in a recent review paper by Marsiglio and Carbotte [10].

BCS theory was very successful in explaining the isotope effect, penetration depth, specific heat, NMR relaxation rates, the energy gap in the electronic spectrum and other experimental results for conventional superconductors like Al, Pb, V, Nb, Ta, Cu, including superconducting alloys such as Nb₃Sn. Later it was also applied successfully to the pairing states in ³He, nuclear matter and elementary particle physics. The success of the BCS theory in describing the universality of various properties of all superconductors rested on a simplified model of EP interaction, which captured the essential physics. BCS assumed that the effective phonon-mediated interaction energy between two electrons (or quasiparticles) with wave vectors \mathbf{k} and \mathbf{k}' was negative and a constant ($= -V$, say), for \mathbf{k} and \mathbf{k}' lying within a rim of width $2\hbar\omega_D$ about the Fermi surface and zero otherwise. The constant V was fitted to the transition temperature T_c . The theory predicted both the energy gap and T_c to be proportional to the Debye (or characteristic phonon) frequency

ω_D , thus explaining the isotope effect as well. It is important to recognize that the above BCS model, coupled with the idea of electron pairing, works without any reference to the physical origin of the attractive interaction. Interactions mediated via exchange of excitations other than phonons may very well be responsible for superconductivity in organic or heavy fermion systems and other *unconventional* superconductors. In particular, the discovery of a new class of ceramic oxide superconductors in 1986 [26] has almost certainly shown that BCS-like theories based on the idea of phonon-mediated attractive interaction between electrons are not applicable in these cases, and new theoretical concepts will be required, although phonons may still play a significant role. Currently, the record holder is $\text{HgBa}_2\text{Ca}_2\text{Cu}_3\text{O}_{8+\delta}$ with a $T_c = 133$ K at room pressure. The critical temperature can be raised under pressure to 164 K at about 30 GPa. There are strong indications that magnetic interactions play an important role in these materials, but so far there is no consensus on the mechanism, and the search for an explanation continues.

Even for conventional superconductors the weakness of the BCS model, due to ignoring the details of EP interaction, soon became clear, as metals like Pb and Hg showed noticeable differences from the standard BCS predictions [27]. These differences could not be accounted for by simply arguing that the so-called weak coupling limit $N(0)V \ll 1$ ($N(0)$ being the single-spin electron density of states at the Fermi level), which leads to some universal features in the properties of all superconductors, did not apply to superconductors such as Pb or Hg. There are two reasons why the BCS results are not in complete agreement with measurements [8, 9, 28]. First, the interaction between electrons mediated by phonons is retarded in time. A 'hand waving' argument often used as a qualitative explanation of this retarded interaction is as follows: Suppose an electron passes through a region, attracting nearby positive ions. The ions respond to the electron by performing simple harmonic motion with a characteristic phonon frequency ω_D . It requires a time $t = \pi/2\omega_D$ for the ions to reach the maximum displacement from their equilibrium positions. The second electron feels the polarized lattice and is attracted to where the first electron used to be. Thus, the smaller the characteristic phonon or Debye frequency ω_D the longer the retardation that can be expected. The BCS model, based on time-independent interaction, fails to capture this aspect of the underlying physics. The second problem arises from the finite life-time or the damping of the quasiparticle states. The electrons in the BCS theory should be understood as quasiparticles in the sense of the Landau quasiparticle theory, where it is assumed that the low-lying excited states of a metal or an interacting Fermi gas can be described by a set of long-lived quasiparticles. In the BCS theory these quasiparticles have two residual interactions: the screened Coulomb

interaction and the interaction mediated via virtual phonons. The latter can cause a substantial damping of the quasiparticle states in metals like Pb and Hg so that well-defined quasiparticles no longer exist. As a result the Landau theory cannot be applied for temperatures of the order of $\theta_D = \hbar\omega_D/k_B$. This causes the deviations from the predictions of the BCS theory to be larger for systems with smaller ω_D and higher T_c .

By using the Feynman-Dyson Green's function perturbation theory, Migdal [29, 30] showed that the EP problem for a normal metal can be solved to high accuracy even in the case of strong damping of the quasiparticle states, as long as the parameter $N(0)\theta_D$ or the ratio of the phonon energy and the Fermi energy is small. Eliashberg [31–33] applied Migdal's technique to electrons in a superconductor, using a formalism given by Gorkov [34]. An extension of the Eliashberg theory to include Coulomb interaction between the electrons was given by Morel and Anderson [35] and Scalapino *et al.* [36]. For a comprehensive discussion of the Eliashberg theory readers can consult the review article by Scalapino [27]. In Eliashberg theory Green's functions computed for the BCS-Bogoliubov ground state are used as the zero-order approximation, and the temperature-dependence of superconducting gap and other properties are addressed by using thermodynamic electron and phonon Green's functions [37]. The central quantity of this theory is the so-called Eliashberg function, which expresses the EP interaction in the form of a spectral density. For phonon-mediated superconductivity it forms the essential bridge between theory and experiment in two complementary ways. It can be calculated from *first principles* and used as the key input in the Eliashberg gap equations to determine T_c and the temperature-dependence of the energy gap as well as other properties of the superconducting state. It can also be derived from experiment by the inversion of tunneling spectra, which, in addition to forming the input into the gap equation for further studies, provides a test for the accuracy of theoretical calculations. Density functional theory (DFT) [38, 39] has been very successful in calculating the electronic ground state [40] and vibrational properties [41]. Therefore, not surprisingly, DFT has also been used to calculate the Eliashberg function and EP coupling constant. The remainder of this review will focus on this application of DFT, present some theoretical details and highlight a few selected successful applications of the method. Eliashberg theory has been very successful in describing superconductivity in many conventional metals [9] and provides the starting point for a microscopic description of the mechanism.

Much of the research activities in superconductivity in the past decade have focused on high T_c superconductors. However, the interest in EP-mediated superconductivity was renewed in 2001 with the discovery of superconductivity

in the simple metal MgB₂ with an unexpectedly high T_c of about 40 K [42]. Now, after several years of intense experimental and theoretical investigations, the main features of superconductivity in MgB₂ seem to be well understood and accepted as being due to a phonon-mediated mechanism with different coupling strengths to the electronic σ - and π -bands [43], which leads to the appearance of two distinct superconducting gaps [44]. At present, MgB₂ appears to be the first system for which multi-band superconductivity has been verified independently by several experimental techniques.

2. Electron-phonon coupling and the Eliashberg function

Eliashberg theory, valid despite strong damping of the quasiparticle states, takes into account the retarded nature of EP interaction and is accurate to order $(m/M)^{1/2}$, the square root of the electron to ion mass ratio. Equations of the Eliashberg theory can be formulated in terms of both real and imaginary frequency axes. In the real axis formulation the superconducting gap Δ is complex and defined for all frequencies ω , while on the imaginary axis the gap is real and only defined on the discrete set of imaginary Matsubara frequencies $\omega_n = \pi T(2n - 1)$, with T being the temperature in energy units. The two formulations become formally equivalent by an analytic continuation of the gap and gap equations [9]. Two of the central equations in the imaginary frequency formulation are coupled non-linear equations for the Matsubara gaps $\Delta(i\omega_n)$ and the renormalization factor $Z(i\omega_n)$.

For an isotropic system these two equations take the form (see, e.g., Ref. [8, 9]):

$$\begin{aligned} Z(i\omega_n) &= 1 + \frac{\pi T}{\omega_n} \sum_m \lambda(n-m) \frac{\omega_m}{\sqrt{\omega_m^2 + \Delta^2(i\omega_m)}} \\ Z(i\omega_n)\Delta(i\omega_n) &= \pi T \sum_m^{|\omega_n| \ll \omega_c} [\lambda(n-m) - \mu^*(\omega_c)] \frac{\Delta(i\omega_m)}{\sqrt{\omega_m^2 + \Delta^2(i\omega_m)}}, \end{aligned} \quad (1)$$

where $\mu^*(\omega_c)$ is the Coulomb pseudopotential. ω_c is a cut-off frequency, usually chosen ten times the maximum phonon frequency: $\omega_c \simeq 10\omega_{ph}^{\max}$. The cutoff is very important here, for otherwise the sums will not converge. The EP contribution is contained in

$$\lambda(n-m) = \int_0^\infty \frac{d\omega^2 \alpha^2(\omega) F(\omega)}{(\omega_n - \omega_m)^2 + \omega^2}, \quad (2)$$

where $\alpha^2(\omega)F(\omega)$ is the Eliashberg spectral function. This key quantity of the Eliashberg theory is defined as

$$\alpha^2 F(\omega) = \frac{1}{N(0)} \sum_{\mathbf{k}, \mathbf{k}', ij, \nu} |g_{\mathbf{k}, \mathbf{k}'}^{ij, \nu}|^2 \delta(\varepsilon_{\mathbf{k}}^i) \delta(\varepsilon_{\mathbf{k}'}^j) \delta(\omega - \omega_{\mathbf{k}-\mathbf{k}'}^{\nu}). \quad (3)$$

A related quantity, useful for the study of the influence of EP coupling on the transport properties, is the transport Eliashberg function [13, 45]

$$\alpha_{tr}^2 F = \frac{1}{2N(0)\langle v_F^2 \rangle} \sum_{\mathbf{k}, \mathbf{k}', ij, \nu} |g_{\mathbf{k}, \mathbf{k}'}^{ij, \nu}|^2 (\vec{v}_F(\mathbf{k}) - \vec{v}_F(\mathbf{k}'))^2 \times \delta(\varepsilon_{\mathbf{k}}^i) \delta(\varepsilon_{\mathbf{k}'}^j) \delta(\omega - \omega_{\mathbf{k}-\mathbf{k}'}^{\nu}). \quad (4)$$

In Eqs. (3) and (4), $g_{\mathbf{k}, \mathbf{k}'}^{ij, \nu}$ is the EP matrix element, with ν being the phonon polarization index and \mathbf{k}, \mathbf{k}' representing electron wave vectors with band indices i , and j , respectively. $\varepsilon_{\mathbf{k}}^i$ denotes the band energy of an electron of wave vector \mathbf{k} in the i^{th} band, measured with respect to the Fermi energy E_F . The subscript F denotes the Fermi surface, the angular brackets denote the Fermi surface average, and v_F denotes the Fermi surface velocity. The sums in Eqs. (3) and (4) involve two Fermi surface sums (integrals): one is over the initial electron states \mathbf{k} , the other over the final states \mathbf{k}' . The process involved describes the scattering of an electron on the Fermi surface, with a transfer of crystal momentum $\mathbf{k} - \mathbf{k}'$ to a phonon of frequency $\omega_{\mathbf{k}-\mathbf{k}'}^{\nu} = \omega$. $g_{\mathbf{k}, \mathbf{k}'}^{ij, \nu}$ is the matrix element, i.e. the probability amplitude, for this process.

If the Eliashberg function is known, then a simple integration gives the total EP coupling constant

$$\lambda = 2 \int_0^{\infty} \frac{d\omega}{\omega} \alpha^2(\omega) F(\omega). \quad (5)$$

A detailed derivation of Eliashberg theory would be beyond the scope of this work, and we refer the reader to excellent reviews in the literature [8, 9, 27].

The ultimate goal of a predictive theory of superconductivity would be the ability to calculate the critical temperature without any experimental input for a given material. Unfortunately, the Eliashberg theory still contains one unknown parameter, the so-called Coulomb pseudopotential μ^* . The screened Coulomb repulsion between the two electrons attracted to each other via emission and absorption of virtual phonons is represented by a dimensionless quantity: $\mu = \langle N(0) V_c^{\mathbf{k}\mathbf{k}'} \rangle_{FS}$ where $V_c^{\mathbf{k}\mathbf{k}'}$ is screened Coulomb interaction between the electrons in states (i, \mathbf{k}) and (j, \mathbf{k}') and the subscript denotes the Fermi surface average. Due to retardation (the second electron is attracted to

where the first electron used to be, roughly a quarter of a lattice vibration earlier) and other effects, the effective Coulomb interaction is substantially weakened and μ is renormalized to a much lower value μ^* . Under some approximations, μ^* [8, 35, 36] is given by

$$\mu^*(\omega_c) = \frac{\mu}{1 + \mu \ln(E/\omega_c)}, \quad (6)$$

where E is a characteristic electron energy typically of the order of the plasma frequency ω_{pl} . In principle, this μ can also be calculated. However, the computational task is numerically very demanding. For this reason μ is often used as a free parameter to fit the experimental value of T_c . However, recently there has been progress in developing a treatment of superconductivity based purely on density functional theory, which does not require any empirical input to calculate T_c . This theory treats electrons and nuclei on the same footing and includes the retardation effect directly in the calculations [46, 47].

Eliashberg equations (1) can be solved iteratively from the knowledge of the Eliashberg spectral function. The critical temperature can be identified by the opening of the gap in the electronic spectrum, that means a non-vanishing order parameter Δ . One way to calculate the critical temperature is to assume that at or close to T_c the square of the gap function, being close to zero, can be neglected. This converts the problem into the solution of a simple eigenvalue problem, with T_c being the highest temperature at which the largest eigenvalue is unity. There are efficient algorithms [48], e.g. the power method, that can be used to calculate the largest eigenvalue and the corresponding eigenvector.

Analytic expressions for T_c in terms of the EP coupling constant λ and the Coulomb pseudopotential μ^* can be obtained from the Eliashberg equations (1) under some approximations. For example, a two square-well model [49]:

$$\lambda(n - m) = \begin{cases} \lambda & \text{if both } |\omega_n|, |\omega_m| < \omega_c \\ 0 & \text{otherwise,} \end{cases} \quad (7)$$

along with the neglect of the gap functions in the denominator, leads to [8, 9]

$$T_c = 1.13 \hbar \omega_c \exp \left[-\frac{1 + \lambda}{\lambda - \mu^*} \right]. \quad (8)$$

This equation reduces to the BCS equation for T_c ,

$$T_c = 1.13 \hbar \omega_c \exp \left[-\frac{1}{N(0)V} \right], \quad (9)$$

for the case where $\lambda \ll 1$ and is approximated by $\lambda = N(0)V$, with V being the pairing interaction strength in the BCS model.

McMillan [50] considered the integral equations for the normal and pairing self-energies in the real frequency formulation of the Eliashberg theory, involving the complex gap function $\Delta(\omega)$. By considering the trial gap function

$$\Delta_t(\omega) = \begin{cases} \Delta_0 & 0 < \omega < \omega_0 \\ \Delta_\infty & \omega_0 < \omega, \end{cases}$$

where ω_0 is the maximum phonon frequency, he was able to show that approximate solutions for the critical temperature can be written in the form

$$T_c = \omega_0 \exp \left\{ -\frac{(1 + \lambda)}{\lambda - \mu^*(1 + (\langle \omega \rangle / \omega_0) \lambda)} \right\}, \quad (10)$$

with $\langle \omega \rangle$ being the average phonon frequency, defined as

$$\langle \omega \rangle = \int_0^{\omega_0} \alpha^2(\omega') F(\omega') d\omega' / \int_0^{\omega_0} \frac{d\omega'}{\omega'} \alpha^2(\omega') F(\omega'). \quad (11)$$

Via extensive numerical solutions of the integral equations, McMillan [50] was further able to show that in most cases T_c could be reproduced reasonably well via the expression

$$T_c = \frac{\Theta_D}{1.45} \exp \left\{ -\frac{1.04(1 + \lambda)}{\lambda - \mu^*(1 + 0.62\lambda)} \right\}, \quad (12)$$

where Θ_D is the Debye temperature. The Coulomb pseudopotential μ^* used in the McMillan equation is different from the one that applies to the Eliashberg equation (1). McMillan also showed that the EP coupling constant λ , given by Eq.(5), can be written in the form $\lambda = N(0) \langle I^2 \rangle / M \langle \omega^2 \rangle$, where $\langle I^2 \rangle$ is a mean square electron-phonon (ion) matrix element [50], and the mean square average phonon frequency $\langle \omega^2 \rangle$, with $M \langle \omega^2 \rangle$ acting as an effective spring constant, is defined the same way as implied by Eq.(11). The McMillan formula (Eq.(12)) has been widely used to estimate T_c from calculated values of λ , with μ^* considered as a fitting parameter which typically lies in the range 0.1 – 0.2. Conversely, it has also been used to estimate λ from experimental values of T_c .

The McMillan formula is based on 22 numerical solutions of the Eliashberg equations for $0 \leq \mu^* < 0.25$ and $0 < \lambda < 1.5$, using a single shape for $\alpha^2 F$ function patterned after the phonon density of states in Nb. Allen and Dynes [8, 49, 51, 52] considered results of more than 200 such numerical solutions for a number of different shapes of the Eliashberg function and values of λ from small to as large as 10^6 to propose an expression the same as McMillan's, but with the prefactor $\Theta_D/1.45$ replaced by $\omega_{\text{in}}^{\text{ph}}/1.2$. The logarithmically averaged characteristic phonon frequency $\omega_{\text{in}}^{\text{ph}}$ in the Allen-Dynes formula is obtained from

$$\omega_{\text{in}}^{\text{ph}} = \exp \left\{ \frac{2}{\lambda} \int_0^{\infty} \frac{d\omega}{\omega} \alpha^2(\omega) F(\omega) \ln \omega \right\}. \quad (13)$$

Despite their simplicity and practical success, analytic expressions such as the McMillan or the Allen-Dynes formula above suffer from a severe limitation. While T_c reaches a maximum for $\lambda \rightarrow \infty$ in these analytic expressions, there is no maximum in the exact solution of the Eliashberg equations. Using an Einstein phonon with frequency ω_E , one can derive an asymptotic solution valid for large λ that gives $T_c = 0.183\sqrt{\lambda}\omega_E$ [9]. However, an unlimited increase of λ will lead to lattice instabilities driven by the phonon softening that inevitably accompanies strong EP coupling. By now it is accepted that the critical temperature for EP superconductivity is limited by lattice stability arguments and not by the mathematical structure of the theory [7–9].

2.1. Eliashberg function from experiment: Inversion of tunneling spectra

The most direct experimental probe of the EP interaction in superconductors is via the tunneling of single particle states. It was first pointed out by Schrieffer, Scalapino and Wilkins [53] (see also Rowell, Anderson and Thomas [54]) that the electronic density of states in the superconducting state $N_s(\omega)$ is given by

$$\frac{N_s(\omega)}{N(0)} = \text{Re} \left\{ \frac{|\omega|}{\sqrt{[\omega^2 - \Delta^2(\omega)]}} \right\}, \quad (14)$$

and this is measured directly in the superconducting to normal metal tunneling at zero temperature. For a frequency-independent gap the above equation reduces to the familiar BCS result. At finite temperatures $T < T_c$ the ratio of the

derivative of the tunneling current to the applied voltage $\partial I/\partial V$ in the superconducting and normal states gives the ratio in Eq.(14) smeared by the derivative of the Fermi distribution function in the normal metal. At zero (very low) temperature the derivative of the Fermi function reduces to a Dirac delta function, and $N_s(\omega)$ is obtained directly from the derivative of the tunneling current in the superconducting state with respect to the applied voltage:

$$\frac{\partial I_s}{\partial V} = \alpha_T \text{Re} \frac{|\omega|}{\sqrt{\omega^2 - \Delta^2(\omega)}} \Big|_{\hbar\omega=eV}, \quad (15)$$

where the factor α_T is determined by the properties of the tunneling barrier and the corresponding average of the Fermi velocities of quasiparticles. Knowing the spectral function $\alpha^2(\omega)F(\omega)$ and the Coulomb pseudopotential μ^* , one can solve the Eliashberg gap equations and obtain the tunneling density of states or the left hand side of Eq.(14). McMillan and Rowell [55, 56] decided to reverse the direction of calculation by starting with the experimentally measured density of states $N_s(\omega)$ and the measured energy gap Δ_0 . Using the knowledge of the tunneling current derivative and thus $N_s(\omega)$, McMillan and Rowell worked backward through the real axis gap equations to obtain $\alpha^2(\omega)F(\omega)$ and μ^* . This procedure has come to be known as the "inversion of the gap equations". It involves repeated solution of the Eliashberg equations, starting with a model $\alpha^2(\omega)F(\omega)$ and adjusting it constantly, along with suitable changes in μ^* , until convergence between predicted $N_s(\omega)$ and the tunneling data is reached. Quite often another property, e.g. the measured energy gap, is used to fit μ^* . The details of the procedure are described by McMillan and Rowell [56], and computer programs to "invert" the gap equations are available [57]. An alternative mathematically elegant method has been discussed in Refs. [9, 58, 59]. The inversion of the gap equation method has been applied to standard superconductors with isotropic (constant in \mathbf{k} space) superconducting gaps, successfully producing Eliashberg spectral functions for many conventional low-temperature superconductors (see e.g. [60]). The method has been used to investigate conventional (low T_c) as well as high-temperature superconductors [61].

Unfortunately, the above approach is restricted to momentum-independent s -wave order parameters and cannot be used to describe anisotropic superconductors such as MgB_2 . In fact, tunneling experiments produce a single function $I(V)$, whereas in the framework of the two-gap model (see discussion in subsection 3.3) one has to determine from this single function $I(V)$ three spectral functions $\alpha^2 F_{\sigma\sigma}(\omega)$, $\alpha^2 F_{\sigma\pi}(\omega)$ and $\alpha^2 F_{\pi\pi}(\omega)$ (the function $\alpha^2 F_{\pi\sigma}(\omega)$ is not independent), which is an impossible task. However,

with the use of calculated Eliashberg functions $\alpha^2 F_{\sigma\sigma}(\omega)$, $\alpha^2 F_{\pi\sigma}(\omega)$, $\alpha^2 F_{\pi\pi}(\omega)$ it becomes possible to compute the tunneling spectrum, and this allows for a direct comparison with experiment [62].

2.2. Theory: *Ab initio* calculations

Calculations of phonon spectra using *ab initio* electronic structure methods have been carried out since the mid-seventies and can be put into two categories: “direct” and “linear response” calculations. In direct calculations, also referred to as “frozen phonon” or “supercell” method, one calculates the difference in the total energy of the crystal in equilibrium configuration and in a distorted state, corresponding to a phonon of a particular wave vector. The frequency can be obtained from a series of calculations involving small displacements of atoms from their equilibrium configuration. Linear response calculations are based on calculating the change in charge density and potential to linear order in the perturbation introduced by a phonon. Relative advantages and disadvantages of these two approaches have been discussed by several authors (see, for example, articles in [63, 64] and Refs. [12, 41]). Although the basic idea underlying the “frozen phonon” approach had been known for a long time and was pointed out casually in a review article by Heine and Weaire [65], a lack of the required accuracy in the electronic structure calculations prevented the method from being used until the mid-seventies. The first such attempt, made by Chadi and Martin [66] in 1976, showed that the “frozen phonon” energies are not lost in the round-off errors of the energy difference between the distorted and undistorted crystals. However, their energy evaluation itself, based on empirical tight-binding parameters, proved to be somewhat unreliable. With improvement in accuracy of calculations, Martin and co-workers were able to apply the method with considerable success (see references in [63, 64]). Linear response calculations can be divided into two groups as well [67]: the dielectric matrix approach and the Sternheimer approach. In the former, the response of the perturbation to the total potential is obtained from the inverse of the dielectric matrix [63], and the perturbation need not be of any given periodicity. In the Sternheimer approach, one starts from a set of self-consistent relations for wave function, charge density and potential and calculates the change in the charge density and total (external+induced) potential to linear order in the perturbation of a given wave vector \mathbf{q} . To linear order, perturbations due to different wave vectors or periodicity can be treated independently of each other, with a numerical workload which, for each wave vector, is of the same order as the self-consistent calculation for the unperturbed system.

Progress in *ab initio* calculations of the EP coupling and particularly of the Eliashberg spectral function was slower than in the calculation of the

phonon spectra. Early calculations of the EP coupling constant was based on the McMillan relation $\lambda = N(0) \langle I^2 \rangle / M \langle \omega^2 \rangle$, where the mean square EP matrix element $\langle I^2 \rangle$ was calculated by using a single scatterer picture and by considering the change in the original (non-self-consistent) potential due to movement of the ion which is supposed to scatter the electron [68]. Such calculations, known as the rigid-ion approximation (RIA) or rigid muffin-tin approximation (RMTA), were reasonably successful for transition metals and even some alloys (see Chapter 7 in Ref. [1] for a review of these calculations and results). Alternative approaches used the McMillan procedure for the inversion of the tunneling data to obtain the Eliashberg function or simply assumed the latter to be proportional to the phonon distribution [9]. During the eighties Cohen and co-workers [69–73] studied several superconductors by employing *ab initio* pseudopotentials and computing the wave vector-dependent EP coupling constant from self-consistent change in one-electron potential due to "frozen phonons". Around the same time Weber [74–76] performed the first semi-first-principles calculations of the Eliashberg spectral function and the EP coupling constant λ using non-orthogonal tight-binding parametrization of first-principles APW (augmented plane wave) energy bands.

During the mid-nineties Savrasov [11, 13] used the full potential linear muffin-tin orbitals (FP-LMTO) method and calculated the phonon spectra, Eliashberg function and the EP coupling constant in the framework of linear response theory by solving self-consistently the Sternheimer equations resulting from the first order change in potential and charge density due to perturbations corresponding to phonons of given wave vectors. Such calculations have also been carried out using *ab initio* pseudopotentials and plane-wave basis (PWSCF) [77–79].

Recently an *ab initio* theory of superconductivity [46, 47] has been developed, where the fundamental quantities are the ordinary electron density, the superconducting order parameter, and the diagonal nuclear N -body density matrix. The former two quantities are determined by Kohn-Sham equations, while the nuclear density matrix follows from the Schrödinger equation with an effective N -body interaction. This theory, developed within a formally exact density functional framework, has been used to calculate Eliashberg spectral functions and other superconducting properties of elemental solids Al, Mo, Ta, Pb and Nb [47].

2.3. Coulomb pseudopotential

A reliable *ab initio* calculation of the Coulomb pseudopotential μ^* entering the Eliashberg equation (1) is difficult [8], as there is no small

parameter that allows for a suitable perturbation theory to be developed for the Coulomb interaction between electrons. Fortunately, its magnitude is small compared with the EP coupling constant λ for most conventional superconductors and often within the uncertainties of the calculated values of λ itself. Calculation of μ^* must take into account that a large part of the normal state Coulomb energy is already included in the band energies, and must therefore not appear in μ^* . Phenomenological calculations based on approximate treatment of various renormalization effects gives rise to the form given in Eq. (6). First principles density functional calculations of μ^* based on a dielectric matrix approach given by Hybersten and Louie [80] have been carried out by Lee *et al.* [81, 82] and Moon *et al.* [83] for Al, Nb and MgB₂. The results are usually close to those calculated by using the RPA (random phase approximation) screening of the electron gas.

2.4. Computational details: FP-LMTO

As discussed above, traditionally pseudo-potential methods with a plane-wave basis set [41] have been used for the calculation of EP interaction, the motivation being primarily the computational ease that a plane-wave basis provides. However, for strongly covalent materials or materials with narrow localized bands, such methods encounter practical problems related to slow convergence and the requirement of a very large number of plane waves and, thus, large storage. This prompted the search for alternative approaches to the problem. In this paper we focus on the all-electron full-potential linear-muffin-tin-orbital (FP-LMTO) [84–86] method developed by Savrasov *et al.* [11–13], where phonons and EP interactions are calculated using the linear-response scheme based on a solid state generalization [41] of the Sternheimer method [87–89].

In the scheme used by Savrasov *et al.* [11–13] a perturbation of the external (nuclear electrostatic) potential to linear order in the displacement of the ions corresponding to a given wave vector is introduced and first order corrections to one-electron wave functions, charge density and the effective potential (sum of external, Coulomb and exchange-correlation) are calculated. The calculation involves solving the Sternheimer equation, which is the Schrödinger equation including the first order change in the effective potential. Savrasov *et al.* needed to construct a variational solution to the Sternheimer equation, as the unperturbed wave functions and energy bands in the LMTO method are themselves variational solutions, dependent on the basis set. Pulay forces [90], i.e. the forces due to the incompleteness of the basis sets used in the variational solution, had to be carefully accounted for in

the calculation. In addition, in the LMTO method the basis set is not fixed, it changes with the change in the external potential. As a result the change in the wave functions consists of two parts: the standard part involving the first order change of the expansion coefficients in the unperturbed basis and the one involving the first order change in the basis itself. This latter part would be absent in methods using fixed basis sets.

In the approach used by Savrasov *et al.* [11–13] perturbations due to different wave vectors can be treated independently of each other, with a numerical workload which, for each wave vector, is of the same order as the self-consistent calculation for the unperturbed solid. The method avoids the inversion of large matrices required for the calculation of response functions via the dielectric matrix approach, which also involves slowly convergent sums over the excited states of the unperturbed Hamiltonian. As with any other method based on the linear response scheme, the method is not restricted to perturbations of wave vectors commensurate with the lattice as in the “frozen phonon” approach.

Using the FP-LMTO code of Savrasov *et al.* one can calculate the electronic structure of the unperturbed crystal with an accurate multiple- κ - (usually 2- or 3-) *spd* LMTO basis set for the valence bands. The code allows for semicore states, which are treated as valence states in separate energy windows. The charge densities and potentials are represented by spherical harmonics with $l \leq 6$ inside the non-overlapping muffin-tin spheres and by plane waves in the interstitial region. Brillouin zone (BZ) integrations can be performed with the full-cell tetrahedron method [91]. After the self-consistent solutions for the unperturbed crystal are obtained, linear response calculations for the phonon frequencies and wave vectors can be carried out. For the calculation of the Eliashberg spectral functions, the expression in terms of the phonon linewidth $\gamma_{\mathbf{q}\nu}$ as discussed by Allen [92] is employed:

$$\alpha^2 F(\omega) = \frac{1}{2\pi N(0)} \sum_{\mathbf{q}\nu} \frac{\gamma_{\mathbf{q}\nu}}{\omega_{\mathbf{q}\nu}} \delta(\omega - \omega_{\mathbf{q}\nu}) \quad (16)$$

The linewidth, given by the Fermi “golden rule”, is written as

$$\gamma_{\mathbf{q}\nu} = 2\pi\omega_{\mathbf{q}\nu} \sum_{\mathbf{k}, ij} |g_{\mathbf{k}+\mathbf{q}}^{ij,\nu}|^2 \delta(\varepsilon_{\mathbf{k}}^i) \delta(\varepsilon_{\mathbf{k}+\mathbf{q}}^j). \quad (17)$$

The method has been applied successfully [13] to obtain the Eliashberg spectral and transport functions for elemental metals such as Al, Cu, Mo, Nb, Pb, Pd, Ta, and V. The comparison of the theoretical $\alpha^2 F(\omega)$ with the one

obtained from tunneling measurements shows close agreement. Temperature-dependent electrical and thermal resistivities and transport constants λ_{tr} agree well with the experimental data. The authors conclude that the method provides the description of EP interactions in these tested materials with an accuracy of about 10%. Further applications include the transition metal compound NbC [12] and doped high temperature superconductors like CaCuO₂ [93].

3. Case studies

3.1. Elemental superconductors at normal pressure

Savrasov and Savrasov [13] have calculated the phonon spectra and the Eliashberg functions for several elemental superconductors and demonstrated the effectiveness of the FP-LMTO-based linear response method in reproducing these correctly, in close agreement with the experimental results. One important observation made by these authors is that the lattice parameters chosen for the calculation should be those giving the minimum of the calculated total energy. In methods based on the local density approximation (LDA) to DFT these tend to be slightly smaller than the experimental lattice parameters. Phonon frequencies calculated for the experimental lattice parameters usually turn out to be lower than the experimental phonon frequencies, resulting in a slightly higher value of the EP coupling constant. For comparison with experimental phonon frequencies and Eliashberg functions, calculations should thus use theoretical minimum energy lattice parameters. However, for comparison with experimental values of the phonon linewidths, Savrasov and Savrasov [13] recommend using the experimental lattice parameters.

For the sake of the illustration in Fig. 1 we show the phonon distribution functions $F(\omega)$, the Eliashberg spectral functions $\alpha^2 F(\omega)$ and $\alpha^2(\omega)$ (defined as the ratio $\alpha^2 F(\omega)/F(\omega)$) for bcc Nb, and fcc Pd and Pb. The lattice parameter used for fcc Pd is the experimental lattice parameter 7.35 a.u., while for Nb we used the theoretical minimum energy lattice parameter of 6.22 a.u. For Pb a lattice parameter of 9.37 a.u., 0.2% higher than the experimental value, was chosen. The calculations employed a three- κ basis set, and a 32^3 division of the Brillouin zone (BZ) for computing the ground state electronic structure of the undistorted lattice. The dynamical and Hopfield (EP coupling) matrices were computed for 29 wave vectors, corresponding to a 8^3 division of the BZ. The number of wave vectors used in the BZ sums in calculating the Hopfield matrix should be of the order of 1000 in the irreducible BZ. In our calculations it was 897. All calculations

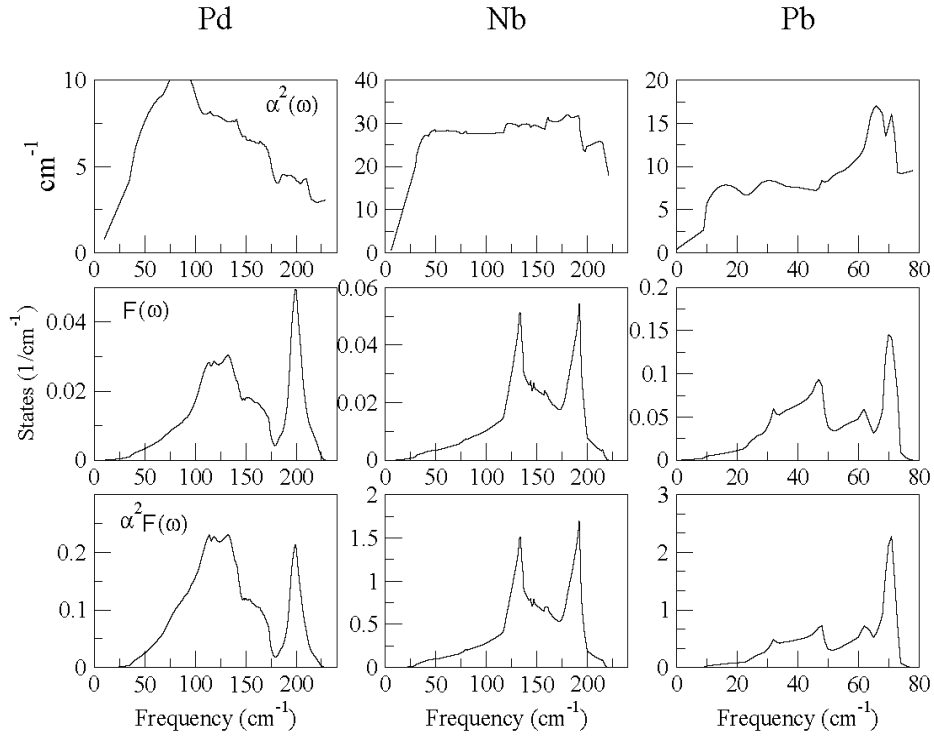


Figure 1. Phonon density of states $F(\omega)$, the Eliashberg spectral function $\alpha^2 F(\omega)$ and the function $\alpha^2(\omega)$, defined as the ratio $\alpha^2 F(\omega)/F(\omega)$, for fcc Pd, bcc Nb and fcc Pb with lattice parameters 7.35 a.u., 6.22 a.u. and 9.373 a.u., respectively.

employed the exchange correlation potential of Janak, Moruzzi and Williams [94], which, because of the absence of spin-polarization, is essentially the same as that of Hedin and Lundqvist [95]. Small differences between the results presented here and those that appeared in the original work of Savrasov and Savrasov [13] are mainly due to different choices of exchange correlation potential and (possibly) the number of wave vectors used in the computations of dynamical and Hopfield matrices.

The function $\alpha^2(\omega)$ has qualitatively different variations with respect to phonon frequency for the three cases shown: for Pb it increases monotonically with frequency, for Nb it remains almost unchanged after an initial increase, while for Pd it decreases monotonically after the initial increase. However, in all cases the structure in the Eliashberg function is determined primarily by the phonon distribution function, lending credibility to earlier calculations (see the article by Scalapino in Ref. [2]) based on models of the Eliashberg functions, where the peak positions and widths were chosen to match the phonon distribution functions obtained from inelastic neutron scattering experiments. In subsections 3.3 and 3.5 we will discuss systems for which such a model becomes invalid. These are systems where most of the EP coupling is via a few phonon modes that couple anomalously strongly to electrons.

Values of the EP coupling constant λ and resulting superconducting transition temperatures T_c for these solids have been discussed by Savrasov [13] (see also Ref. [96]). Of the three cases shown, only Nb and Pb show superconductivity, while superconductivity in Pd is known to be suppressed completely by strong ferromagnetic or antiferromagnetic spin fluctuations (paramagnons). A large density of states $N(0)$ at the Fermi level in fcc Pd causes a large Stoner-enhanced paramagnetic susceptibility, leading to strong spin fluctuations. Calculations of the exchange interactions in fcc Pd for hypothetically enlarged lattice parameters show these to hover between ferromagnetic and antiferromagnetic at the nearest neighbour site [97]. For Pb the calculated EP coupling constant comes out somewhat higher, giving a T_c higher than the experiment. However, the calculated phonon linewidths agree very well with those measured via neutron-resonance spin-echo spectroscopy [98].

3.2. Elemental superconductors at high pressures

At present 29 elements are known to be superconducting at ambient pressure and 23 other elements have been found to become superconducting at high pressure [99]. The effect of pressure on normal superconductors can usually be understood by considering the McMillan expression for the EP coupling constant $\lambda = N(0) \langle I^2 \rangle / M \langle \omega^2 \rangle$. The mean square electron-phonon (ion) matrix element $\langle I^2 \rangle$ increases in general, as the atoms come closer under pressure, while the electron bands broaden, resulting in a decrease in $N(0)$. In general the increase in $\langle I^2 \rangle$ is larger than the decrease in $N(0)$, resulting in a higher value of the Hopfield parameter $\eta = N(0) \langle I^2 \rangle$. Phonon frequencies rise under pressure, and often the higher value of $\langle \omega^2 \rangle$ becomes the dominant factor in determining the pressure effect. As a result of larger $\langle \omega^2 \rangle$ the EP coupling constant λ usually goes down with increasing pressure for normal superconductors. There are systems where $N(0)$ actually goes up under pressure, as a result of new bands starting to cross the Fermi level. One such example is simple cubic phosphorus [100], where T_c rises continuously under pressure between 110 kbar and 210 kbar due to a new band starting to cross the Fermi level, i.e. a new sheet of Fermi surface that appears under pressure and a corresponding increase in $N(0)$. Beyond 210 kbar the stiffening of the phonons results in lowering of T_c . Another prominent example is La, where T_c rises with pressure from around 6 K at ambient pressure, reaching as high as 11-13 K between 6-10 GPa [101]. The increase in T_c with pressure in this system has been interpreted as being due to the increase in the $4f$ density of states at the Fermi level [102] and also to phonon softening [103]. For systems where spin fluctuations play a significant role in the superconducting state, T_c may increase

under pressure due to the suppression of spin fluctuations (all correlation effects, in general) with increasing pressure [104, 105].

Often the application of pressure induces a structural phase transition, and the high pressure superconducting phase has a different crystal structure than the normal pressure phase. For example, silicon exhibits a rich variety of phases [106] under pressure, including a simple hexagonal phase, which is known to be superconducting [107]. Yttrium [108, 109] undergoes several phase transitions under pressure, starting from the ambient pressure hcp phase to a distorted fcc phase around 30-35 GPa. The high pressure phases are superconducting, with T_c rising as high as 19.5 K in the distorted fcc phase. The increase in T_c with pressure has been attributed to an increase in the $4d$ component of the density of states as well as the softening of phonons [109]. An example of an elemental solid where superconductivity under pressure appears without any change in phase is fcc Li, which is essentially a normal metal at ambient pressure, with an upper limit of T_c estimated below 100 μ K. Under pressure the fcc phase becomes superconducting, with T_c reaching as high as 20 K around 35-50 GPa [110–112]. This is attributed to the growth in the size of the necks (similar to those of the Fermi surface of Cu) joining the spherical Fermi surface along the $\langle 111 \rangle$ directions. There is also flattening of the Fermi surfaces between the necks. These necks develop primarily a p -character, transforming Li from an s -electron metal to an $s - p$ metal. The p -character provides some directional (covalent) character to the bonding, which may enhance electron-phonon coupling [113].

There are a large number of organic materials, which become superconducting under pressure. This review addresses superconductivity mediated via EP interaction only and as such will exclude discussion of organic superconductors, where the phonons may not be directly responsible for the superconducting state. In this section we will discuss two elemental solids which have received attention recently: hcp Fe and boron under pressure.

3.2.1. Superconductivity in hcp Fe under pressure

Shimizu *et al.* [114] (see also Refs. [115, 116]) reported resistivity and magnetization measurements on Fe samples under pressure, and identified a superconducting phase characterized by both the Meissner effect and the vanishing of the resistivity above a pressure of 15 GPa. At such pressures the stable crystal structure of Fe is known to be hcp. Mazin *et al.* [117] and Bose *et al.* [118] have reported theoretical calculations in support of the possibility of superconductivity in the high pressure hcp phase of Fe. The work of Mazin *et al.* [117] was based on a RMTA calculation [68] of the Hopfield parameter using the linear augmented plane-wave (LAPW) method, and estimating the average phonon frequency from previous calculations of phonon dispersions

[119, 120] in hcp Fe. Bose *et al.* [118] used the FP-LMTO linear response method to compute the phonon frequencies, Eliashberg functions and the EP coupling constant as a function of the lattice parameter, using a triple- κ *spd* LMTO basis set. The dynamical matrix was generated for 28 phonon wave vectors in the irreducible BZ, corresponding to a mesh of (6,6,6) reciprocal lattice divisions. The BZ integration for the dynamical matrix was done for a mesh of (12,12,12) reciprocal lattice divisions, and that for the EP (Hopfield) matrix was done for a (24,24,24) mesh. Exchange and correlation were treated via the generalized gradient approximation (GGA) of Perdew *et al* [121]. Their results for phonon frequencies are in good agreement with the results of Alfé *et al.* [120]. In Fig. 2 we show the phonon spectrum and density of states, Eliashberg spectral and transport functions for hcp Fe at a lattice parameter of 4.6 a.u. and c/a ratio of ideal hcp structure. The smooth solid lines in Fig. 2 correspond to spline fits to the calculated frequencies (solid circles). Due to the small number of calculated frequencies the shapes of the lines representing the bands near the zone boundaries could be incorrect. The connections of the calculated points with lines and band crossings in Fig. 2 were determined by examining the phonon eigenvectors. However, the number of wave vectors considered along each symmetry direction was at most four and often less. Thus, the possibility of errors in band crossings cannot be ruled out.

The FP-LMTO equilibrium (minimum energy) lattice parameter for hcp Fe with $c/a = \sqrt{8/3}$ is 4.615 a.u. Bose *et al.* [118] carried out the FP-LMTO linear response calculations for ideal hcp Fe for six lattice parameters: 4.7, 4.6, 4.5, 4.4, 4.2 and 4.4 a.u. In Fig. 3 we show the phonon density of states and the corresponding Eliashberg spectral function $\alpha^2F(\omega)$ for reduced lattice parameters 4.5, 4.4 and 4.0 a.u.

In Table 1 we have reproduced the results of Bose *et al.* for the various lattice parameters. Results for lattice parameter 4.7 a.u. are included merely for comparison with other lattice parameters, and not for comparison with experiment. The strong EP coupling (stronger than that at $a = 4.6$ a.u.) is of no experimental consequence, since (i) at this lattice parameter the system is at a negative pressure, not accessed by experiment; and (ii) our theoretical calculations show that at this expanded volume the system is most likely antiferromagnetic. In Table 1 T_c^{calc} was calculated by solving the Eliashberg equation (Eq.(1)) and T_c^{McM} was calculated by using the Allen-Dynes form of the McMillan Equation (Eq.(12)) with the prefactor $\Theta_D/1.45$ replaced by $\omega_{ln}^{ph}/1.2$. The cutoff frequency ω_c used for the Eliashberg equation was chosen to be 10 times the maximum phonon frequency. The choice of the Coulomb pseudopotentials $\mu^*(\omega_c)$ and $\mu^*(\omega_{ln})$ for the Eliashberg and McMillan equations, respectively, is discussed in detail in Bose *et al* [118].

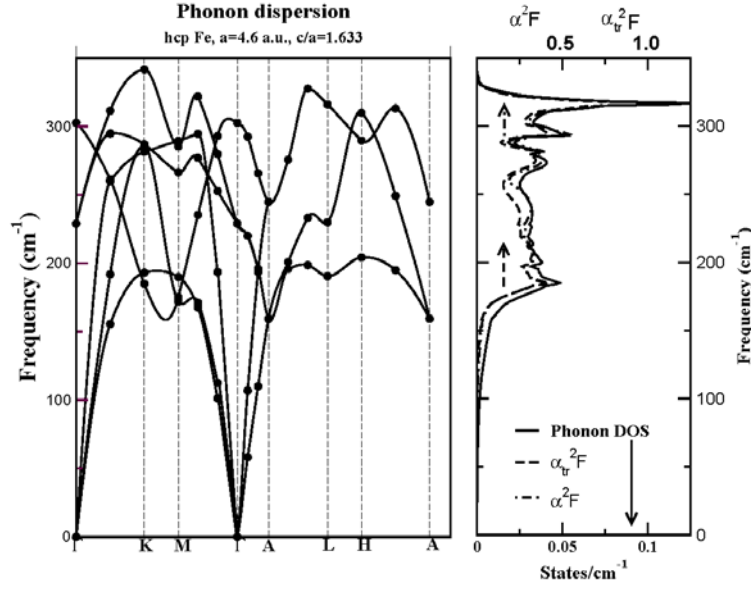


Figure 2. Phonon spectrum, density of states and the Eliashberg spectral function α_F^2 and the transport Eliashberg function $\alpha_{tr}^2 F$ for ideal ($c/a = \sqrt{8/3}$) hcp Fe at the lattice parameter 4.6 a.u. [118]. The equilibrium (minimum energy) lattice parameter is 4.615 a.u.

Table 1. FP-LMTO linear response results for the pressure P , Hopfield parameter η , mean square electron-ion matrix element $\langle I^2 \rangle$, plasma frequency ω_{pl} , average phonon frequency ω_{ln}^{ph} , and the EP coupling parameter λ for various lattice parameters a of ideal hcp Fe [118]. η (RMT/RAS) is the Hopfield parameter obtained by using the rigid muffin-tin (atomic sphere) approximation. T_c^{calc} and Δ_0 are the critical temperature and the zero temperature energy gap, respectively, obtained by solving the Eliashberg equation with a cutoff frequency ω_c and Coulomb pseudopotential $\mu^*(\omega_c)$. T_c^{McM} is the critical temperature obtained from the McMillan formula (12) using Coulomb pseudopotential $\mu^*(\omega_{ln})$.

a	a_B	4.0	4.2	4.4	4.5	4.6	4.7
P	GPa	350	162	56	26	2.3	-14
η	Ry/bohr ²	0.268	0.368	0.229	0.139	0.111	0.099
η (RMT/RAS)	Ry/bohr ²	0.214	0.167	0.124	0.108	0.095	0.088
$\langle I^2 \rangle$	(Ry/bohr) ²	0.056	0.063	0.032	0.018	0.013	0.010
ω_{pl}	eV	10.30	8.82	7.68	7.21	6.78	6.40
ω_{ln}^{ph}	cm ⁻¹	K 640	542	439	372	336	295
ω_c	cm ⁻¹	445	376	305	258	233	205
$\mu^*(\omega_c)$		7000	6000	4600	4600	4600	4490
$\mu^*(\omega_{ln})$		0.224	0.224	0.218	0.221	0.224	0.226
λ		0.139	0.138	0.137	0.135	0.134	0.133
T_c^{McM}	K	0.277	0.570	0.538	0.434	0.431	0.508
T_c^{calc}	K	< 0.01	6.37	4.06	1.06	0.94	2.21
Δ_0	cm ⁻¹	$5 \cdot 10^{-7}$	4.52	3.11	0.83	0.66	1.73
$\Delta_0/k_B T_c^{calc}$		< 10^{-6}	7.38	4.63	1.28	0.99	2.54
			2.35	2.15	2.21	2.14	2.30

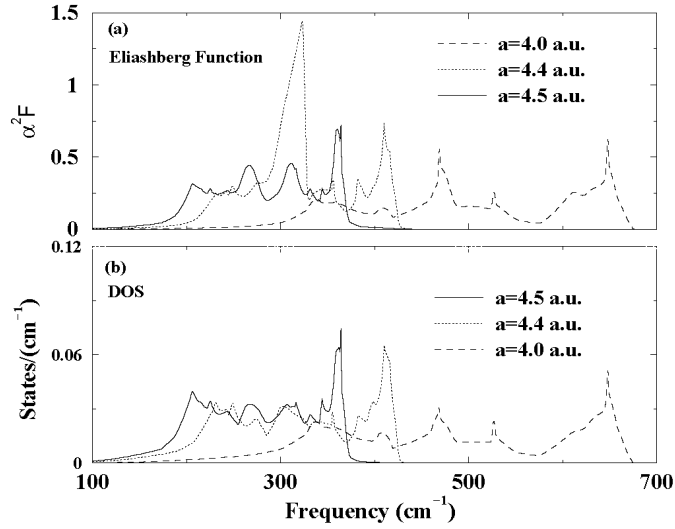


Figure 3. Phonon density of states and the Eliashberg function for hcp Fe for three different lattice parameters ($c/a = \sqrt{8/3}$) [118].

Table 1 also compares the values of the Hopfield parameter obtained via the linear response calculation with those based on the rigid atomic sphere (RAS) approximation, which is equivalent to RMT in the LMTO-ASA (atomic sphere approximation) scheme. It is seen that RAS consistently underestimates the Hopfield parameter, and the extent of the underestimation increases with pressure. Note that the ratio $\Delta_0/k_B T_c$ is about 17-25% higher than the BCS value 1.76.

Because there is a strong possibility [117, 118] that hcp Fe is on the borderline of an antiferromagnetic or a complex (non-collinear) magnetic instability, Bose *et al.* considered the effects of both ferromagnetic and antiferromagnetic spin fluctuations on the transition temperature T_c . In principle, spin fluctuation effects can be incorporated in the linearized Eliashberg equation, Eq.(1), at $T = T_c$ by writing it in the form

$$\begin{aligned}
 Z(i\omega_n) &= 1 + \frac{\pi T_c}{\omega_n} \sum_{n'} W_+(n - n') \text{sign}(n'), \\
 Z(i\omega_n) \Delta(i\omega_n) &= \pi T_c \sum_{n'}^{|\omega_n| \ll \omega_c} W_-(n - n') \frac{\Delta(i\omega_{n'})}{|\omega_{n'}|},
 \end{aligned} \tag{18}$$

where the interactions W_+ and W_- contain a phonon contribution λ , and a contribution from spin fluctuations λ_{sf} . The expressions for the interaction terms are:

$$W_+(n - n') = \lambda (n - n') + \lambda_{sf} (n - n'), \tag{19}$$

and

$$W - (n - n') = \lambda (n - n') - \lambda_{sf} (n - n') - \mu^* (\omega_c), \quad (20)$$

where the EP coupling constant λ is given by Eq.(2). Since the Migdal theorem does not hold for spin fluctuations (paramagnons), it is difficult to derive a formula for λ_{sf} . Invoking analogy with the phonons, one could write the contribution connected with spin fluctuation as

$$\lambda_{sf}(n - n') = \int_0^\infty \frac{d\omega^2 P(\omega)}{(\omega_n - \omega_{n'})^2 + \omega^2},$$

where $P(\omega)$ is the spectral function of spin fluctuations [118]. In the absence of a rigorous justification of the above formula, Mazin *et al.* [117] and Bose *et al.* [118] resorted to ignoring the dependence of λ_{sf} on Matsubara frequency and estimating it approximately from the knowledge of the Stoner parameter. The details regarding the choice of λ_{sf} for ferromagnetic and antiferromagnetic spin fluctuations and the Coulomb pseudopotential $\mu^* = \mu^*(\omega_{ln})$ are given in Ref. [118]. In order to incorporate spin fluctuation effects on T_c , the following Allen-Dynes form of the McMillan formula was used:

$$T_c = \frac{\omega_{ln}^{ph}}{1.2} \exp \left\{ - \frac{1.04(1 + \lambda_{ph} + \lambda_{sf})}{\lambda_{ph} - \lambda_{sf} - \mu^*[1 + 0.62(\lambda_{ph} + \lambda_{sf})]} \right\}. \quad (21)$$

In addition to spin fluctuations, Bose *et al.* examined the effects of magnetic impurities on the conventional *s*-wave superconductivity in hcp Fe. They also considered a simplified model of *p*-wave superconductivity.

Despite some quantitative differences between the LAPW-RMTA results of Mazin *et al.* [117] and the FP-LMTO linear response results of Bose *et al.* [118], the essential conclusions reached by the two studies were the same. The Hop-field parameter η increases steadily with pressure, resulting in an initial increase of T_c . At higher pressure, below volumes of ~ 50 a.u. per atom (above estimated pressures ~ 160 GPa), phonons stiffen rapidly, bringing the T_c down. The rate of decrease in T_c for pressures above ~ 150 GPa is faster in the linear response results of Bose *et al.* [118] than that suggested by the LAPW-RMTA results of Mazin *et al.* [117]. T_c 's based on the *s*-wave EP coupling and maximum possible estimates of μ^* are higher than the experimental values. The range of volume (pressure) where superconductivity appears is much broader in the calculations than what is

observed in the experiments of Shimizu *et al.* [114]. What is surprising is not that hcp Fe is superconducting, but that the observed superconductivity disappears so quickly, as the pressure is increased. Inclusion of ferromagnetic /antiferromagnetic spin fluctuations and scattering from magnetic impurities can all bring the calculated values of T_c down to the range of observed values, but cannot substantially improve the agreement between the calculated and the experimental pressure/volume range of the superconducting phase. The pair-breaking effect of the spin fluctuation and/or magnetic impurities cannot explain the rapid disappearance of superconductivity with pressure. A simplified treatment of p-wave pairing due to EP and spin fluctuation interactions yields a very small T_c (≤ 0.01 K). It is thus conceivable that superconductivity observed in hcp Fe is spin-mediated rather than phonon-mediated. In order for the EP superconductivity not to be operative in hcp Fe, the hcp phase needs to be magnetic, for which both theoretical and experimental evidence have been claimed in the literature [122–125]. Although the density functional based linear response calculations have not solved the problem of superconductivity in hcp Fe, they have helped in clarifying issues related to EP coupling and pointed to the need for further experiments to ascertain the nature of the magnetic and superconducting state of hcp Fe.

3.2.2. Superconductivity in boron under pressure

Metallization of boron under pressure was predicted on the basis of electronic structure calculations some time ago by Mailhiot *et al.* [126]. According to their calculations, nonmetallic icosahedral boron (B) is expected to undergo a structural transition, first to a body-centered tetragonal (bct) phase at ~ 210 GPa and then to a face-centered cubic (fcc) phase at ~ 360 GPa. Recently high pressure experiments by Eremets *et al.* [127] have found boron to be not only a metal, but also a superconductor at high pressure, with superconducting transition temperature T_c increasing with increasing pressure. Superconductivity appears at around 160 GPa, and T_c increases from 4 K at 160 GPa to 11.2 K at 250 GPa.

Guided by the theoretical results of Mailhiot *et al.* [126], Bose *et al.* [96] examined the possibility of superconductivity in fcc and bct phases of boron at high pressure. As is indicated later in this section, the phase of boron at pressures in the range of 160-250 GPa might not be fcc or bct. Therefore, the results for the bct and fcc phases obtained by Bose *et al.* [96] and presented here are for illustration purpose only. FP-LMTO linear response calculations in the fcc and bct phases yield information regarding the modes that go soft as the phase changes from fcc to bct and from bct to either icosahedral or

some other structure. The correct theoretical description of superconductivity in boron under pressure still remains an open issue.

The FP-LMTO total energy calculations by Bose *et al.* [96] showed the fcc phase to be energetically favourable to the bct phase at very high pressures (volume per atom $< 21.3 \text{ bohr}^3$), estimated to be in excess of 360 GPa. The bct phase (volume per atom $> 21.3 \text{ bohr}^3$) is stable at lower pressures in the range of 360-210 GPa. Pseudopotential calculations of total energy of the bct structure by Mailhiot *et al.* [126] as a function of c/a had indicated a global minimum around $c/a \sim 0.6$. Via an elaborate study of the total energies for various monoclinic and tetragonal distortions of the fcc unit cell as well as the bct total energies for various c/a values, these authors concluded that the bct minimum occurs around $c/a \sim 0.65$. FP-LMTO calculations of Bose *et al.* [96] on a crude mesh of c/a for fixed volumes did indicate a value in the range 0.6–0.7. Their linear response calculations for $c/a = 0.65$, however, produced complex phonon frequencies at the symmetry point N and nearby wave vectors. Increasing c/a to 0.675 resulted in real frequencies at all symmetry and intermediate points. The actual energy values for $c/a = 0.65$ and 0.675 for the same volume in the bct phase were found to be very close. Thus, the linear response calculations of the phonon frequencies and the Eliashberg spectral function for the bct phase were carried out for a c/a value of 0.675.

FP-LMTO linear response calculations of Bose *et al.* [96] for the fcc phase showed that with the lowering of pressure (increasing volume) the X-point transverse phonons become soft first. The transition from the fcc to bct phase with the lowering of pressure is driven by the softening of these phonons, driving the system to a c/a ratio lower than the fcc value of 1.414. Below, in Fig. 4, we show the phonon spectra and the softening of the X-point phonons with increasing volume. The phonon frequencies were calculated for 29 wave vectors in the irreducible part of the Brillouin zone (BZ), resulting from a 8,8,8 division of the BZ. This division of the BZ yields only a small number (3-4) of wave vectors along the high symmetry directions. The solid lines in Fig. 4 should be taken only as a guide to the eye, rather than actual phonon branches with correct branch crossings. With increasing volume, the phonon frequencies soften throughout the Brillouin zone, as expected. However, the softening of the two transverse phonon branches near the X point is most pronounced. According to the calculated phonons, the transition to the bct phase should occur between lattice parameters 4.4 and 4.6 a.u.

The phonon density of states and the Eliashberg spectral functions for three different lattice parameters in fcc B is shown in Fig. 5. The X-point transverse phonons are related to the 180° out of phase vibration of the two atoms in a bct unit cell ($c/a = 1.414$ for fcc lattice). Softening of these phonons

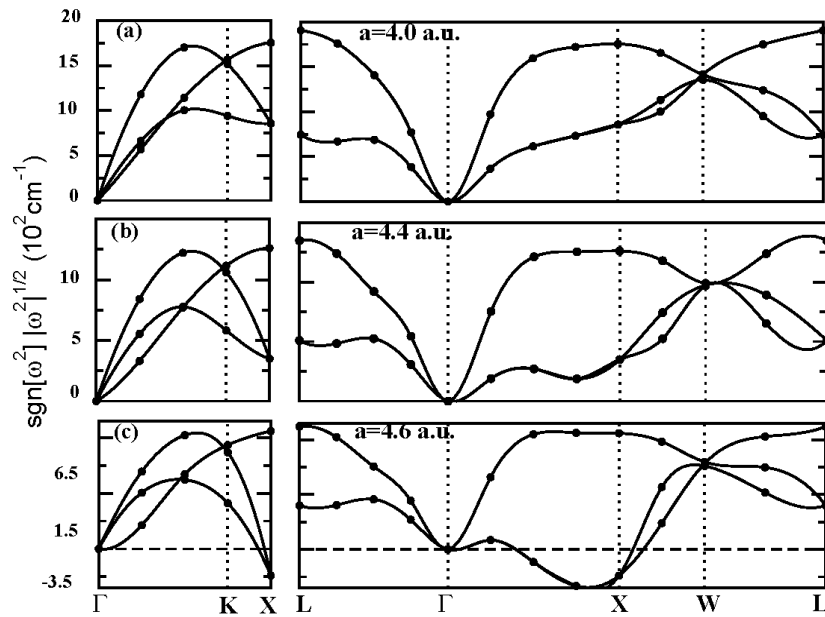


Figure 4. Calculated phonon spectra [96] for fcc B for the lattice parameters (a) $a = 4.0$ a.u., (b) $a = 4.4$ a.u. and (c) $a = 4.6$ a.u. The dots represent the calculated phonon frequencies, with solid lines providing only a guide to the eye. The softening of the transverse phonons at the symmetry point X occurs as the system expands to a volume above $3.4 \text{ \AA}^3/\text{atom}$, consistent with the earlier results of Mailhiot *et al.* [126].

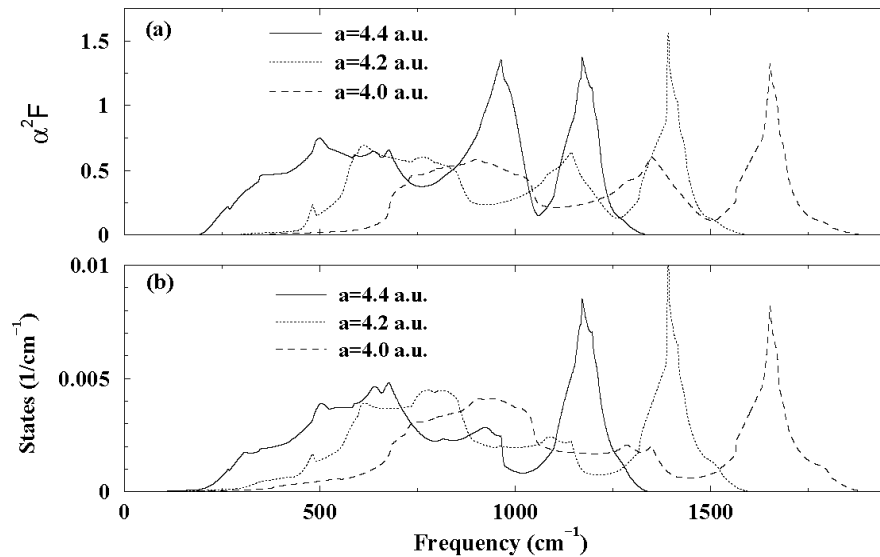


Figure 5. Phonon density of states and Eliashberg spectral function in fcc boron [96].

with increasing volume indicates growing instability of the fcc structure with respect to the c/a ratio, and acts as a precursor to the $\text{fcc} \rightarrow \text{bct}$ phase transition.

This phonon-softening has two important effects: it increases the phonon density of states at low frequencies beyond the usual parabolic DOS given by

the Debye (continuum) model and it increases the EP coupling in the low frequency region (partly due to increased phonon DOS and partly due to increased EP matrix element). These effects are clearly seen in Fig. 5. The sharp peaks in both the density of states and the Eliashberg spectral function at the high end of the spectrum are due to the lack of dispersion in the longitudinal phonon band close to the X point in the Γ -X direction. The lack of dispersion is enhanced as the atoms move further apart with the lattice parameter changing from 4.0 a.u. to 4.2 a.u., giving a higher density of states and consequently higher EP coupling. No such enhancement is observed as the lattice parameter increases from 4.2 a.u. to 4.4 a.u. For the lattice parameter 4.4 a.u., a sharp peak in the Eliashberg spectral function appears around 900 cm^{-1} , most probably due to the strong coupling of the electrons to phonons close to the W point. However, this coupling is seen to grow weaker at smaller lattice parameters.

For the lattice parameters considered, the Eliashberg spectral function appears to follow the phonon density of states faithfully, indicating that there is no single mode that couples anomalously strongly to the electrons.

In Fig. 6, the phonon spectra of bct B for two different lattice parameters and with the c/a ratio of 0.675 are shown. The linear response calculations for the phonon properties were carried out for 30 points in the IBZ resulting from a 6,6,6 division of the BZ. The solid lines in Fig. 6 have been drawn through the calculated frequencies to provide a guide to the eye and should not be interpreted as the actual phonon branches.

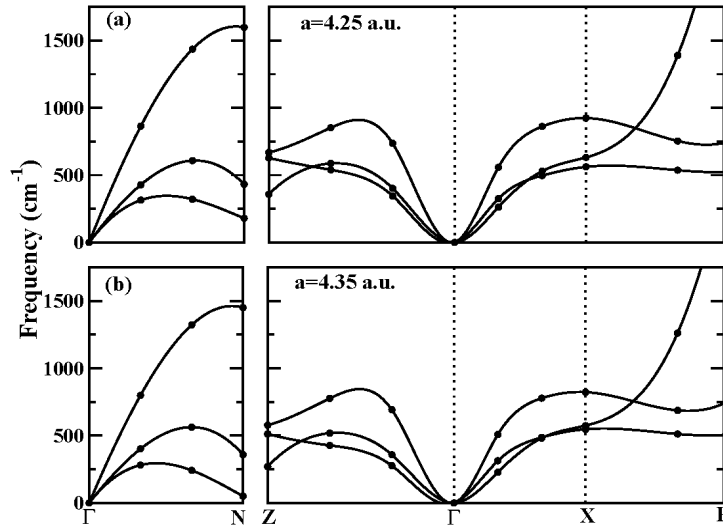


Figure 6. Calculated phonon spectra for bct B [96] for the lattice parameters (a) $a=4.25$ a.u. and (b) $a=4.35$ a.u. for the c/a ratio of 0.675. The dots represent the calculated frequencies, while the solid lines have been drawn through them to guide the eye. For lattice parameters higher than 4.35 a.u. the structure becomes unstable with the N-point transverse phonons becoming soft first.

Bose *et al.* [96] found that with a c/a ratio of 0.675, the bct phase becomes unstable for lattice parameters higher than 4.35 a.u. or volume per atom greater than 27.8 bohr³. This happens with the N-point transverse phonons becoming soft first. With increasing values of the lattice parameter, phonons at other symmetry points become soft as well. Thus, the linear response calculations yield real phonon frequencies only for a small range of volume for the chosen c/a ratio of 0.675. For $c/a = 0.65$, the N-point transverse phonons are found to be imaginary for all lattice parameters corresponding to volumes where the bct phase should be stable according to the FP-LMTO energy-volume curve. Of all the phonons, the ones at the N point are found to be most sensitive to the c/a ratio. In principle, the c/a ratio should be determined for each volume and the lattice parameter. It is likely that the optimum c/a value changes with volume per atom. The c/a value should have some effect on the calculated T_c . FP-LMTO calculations suggest that the c/a ratio should be in the range 0.6-0.7, most probably 0.65 and higher. Hence, it is reasonable to assume that T_c values obtained for optimum values of c/a should not be far from those obtained with $c/a = 0.675$.

In Fig. 7, the phonon density of states and the Eliashberg spectral functions for three different lattice parameters are shown. Unlike in the fcc phase, the bulk of EP coupling is via lower frequency phonons, as most of the spectral weight in Fig. 7(b) comes from the lower half of the allowed frequency range. As in the fcc case, the Eliashberg spectral function and the phonon density of states follow each other closely. There is no disproportionately large contribution from a particular mode.

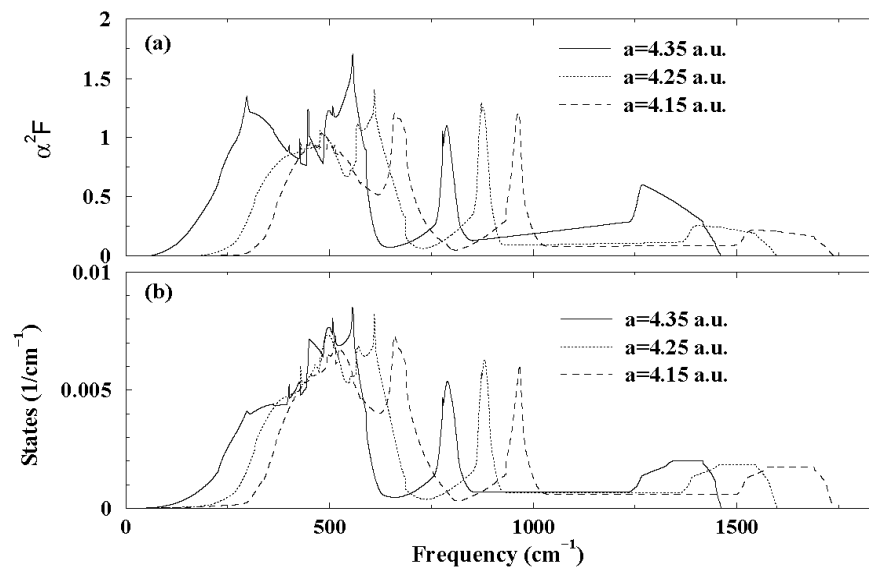


Figure 7. Eliashberg spectral function (a) and phonon density of states (b) for bct B, for three different lattice parameters, and $c/a=0.675$ [96].

Superconducting transition temperatures T_c , calculated by solving the linearized isotropic Eliashberg equation at T_c , for the fcc and bct phases of boron are shown in Table 2. Details of the choice of Coulomb pseudopotential $\mu^*(\omega_c)$ is discussed in detail in Bose *et al.* [96].

As can be seen in Table 2, the results for the fcc and bct phases of boron differ from the experimental results of Eremets *et al.* [127] in two significant ways: first, the transition temperatures T_c in both fcc and bct phases decrease with increasing pressure rather than increase and second, the calculated values of T_c for both phases are too high compared with the experimental values, which lie in the range 4-11.2 K. Note that both the Hopfield parameter η and the phonon frequencies are unusually high (compare with the values for hcp Fe in Table 1), and that this is due to the unusually low values of lattice parameter or inter-atomic distances at these high pressures. Despite unusually high phonon frequencies, T_c is very large due to very large values of the EP matrix element $\langle I^2 \rangle$. The overwhelming possibility appears to be that the phase of boron at pressures applied in the experiments of Eremets *et al.* [127] is neither fcc, nor bct. It is thus crucial to identify the phase of boron at pressures in the range 160-250 GPa, at which the experiments of Eremets *et al.* [127] were carried out. Indeed, there is some theoretical evidence that α -Ga structure [128, 129] might be the appropriate phase of boron that is superconducting. Pseudopotential-based linear response calculation [67, 130]

Table 2. Variation of superconducting transition temperature T_c with volume in the bct and fcc phases of boron [96]. V = volume per atom, ω stands for phonon frequency and $\langle \cdot \cdot \rangle$ s denote averages, $\bar{\omega} = \sqrt{\langle \omega^2 \rangle}$. ω_m is the maximum phonon frequency, η is the Hopfield parameter, and a_0 denotes the bohr radius.

bct Boron							
$V(a_0^3)$	$\omega_m(\text{meV})$	$\bar{\omega}(\text{meV})$	$\langle \omega \rangle(\text{meV})$	$\mu^*(\omega_c)$	$\eta(\text{Ry}/a_0^2)$	λ	$T_c(\text{K})$
20.80	254	153	97	0.297	0.624	1.03	56
24.12	215	123	77	0.289	0.552	1.40	78
25.91	198	110	68	0.285	0.549	1.70	89
26.83	189	70	60.4	0.283	0.562	2.02	97
27.78	181	76.8	42	0.281	0.519	2.73	106
fcc Boron							
$V(a_0^3)$	$\omega_m(\text{meV})$	$\bar{\omega}(\text{meV})$	$\langle \omega \rangle(\text{meV})$	$\mu^*(\omega_c)$	$\eta(\text{Ry}/a_0^2)$	λ	$T_c(\text{K})$
16	236	143	136	0.277	0.926	0.84	50
18.52	199	116	108	0.269	0.752	1.04	67
19.87	183	102	94.4	0.266	0.744	1.31	88
21.30	167	88	77.6	0.262	0.797	1.79	114

by Ma *et al.* [128] provide some evidence that α -Ga boron is indeed superconducting, with T_c possibly in the range that is consistent with the experiments of Eremets *et al.* [127].

3.3. Superconductivity in MgB_2

The high critical temperature of 40 K in the simple binary compound MgB_2 [42] came as an unexpected gift of nature to the scientific community. MgB_2 occurs in the so-called AlB_2 structure (see Fig. 8), which belongs to the hexagonal lattices. The boron atoms form a primitive honeycomb lattice, consisting of graphene-like sheets. These are stacked on top of each other without any displacement and with layers of Mg atoms in between. The base diameter of the hexagonal prisms of the boron atoms is 3.5 Å, roughly equal to the height. This creates large nearly spherical voids, where the Mg atoms can be located. As in graphite, the intraplanar B-B bonds are much shorter than the distance between the planes, hence the B-B bonding is strongly anisotropic.

The band structure of MgB_2 is shown in Fig. 9. There are two π -bands, originating mainly from the two B p_z -orbitals per unit cell. They fill the BZ more or less uniformly, and both of these bands cross the Fermi level. In addition, there are three σ -bands, formed by the three bond-orbitals per cell. Each bond-orbital is primarily the bonding linear combination of the two B sp^2 -hybrids, which are directed along a B-B bond. The lowest σ -band is completely filled, while the other two cross the Fermi level, but only near the Γ point. Near the Fermi level they straddle the Γ -A line with negligible dispersion, giving most of the contribution to both the density of states $N(0)$ and the electron-phonon coupling. These bands form two narrow cylindrical Fermi surfaces around the Γ -A line, while the two π -bands form a three-dimensional tubular network: the third Fermi surface sheet (Fig. 10).

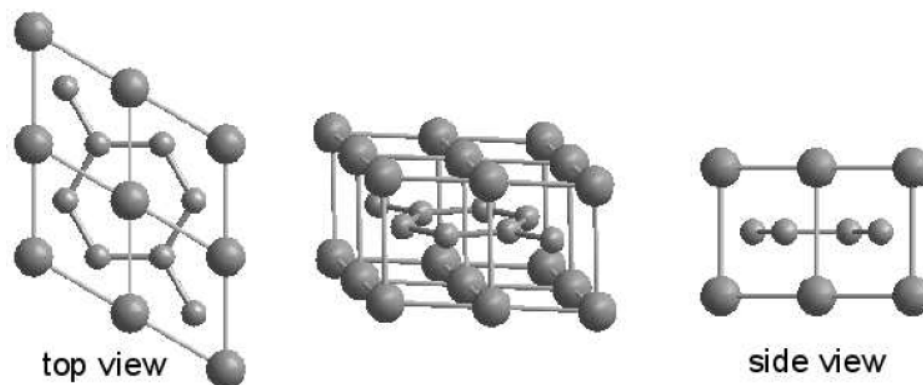


Figure 8. MgB_2 occurs in the hexagonal lattice: the boron atoms (smaller spheres) form graphene-like layers stacked without displacement, with the Mg atoms (larger spheres) located in the voids between.

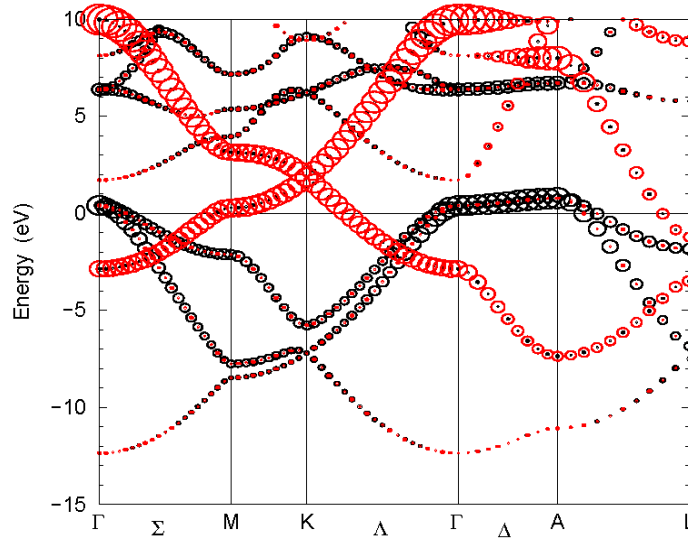


Figure 9. Band structure of MgB_2 with the B p -character. The radii of the red (black) circles are proportional to the Bp_z - (Bp_x, p_y -) character. With kind permission from [43].

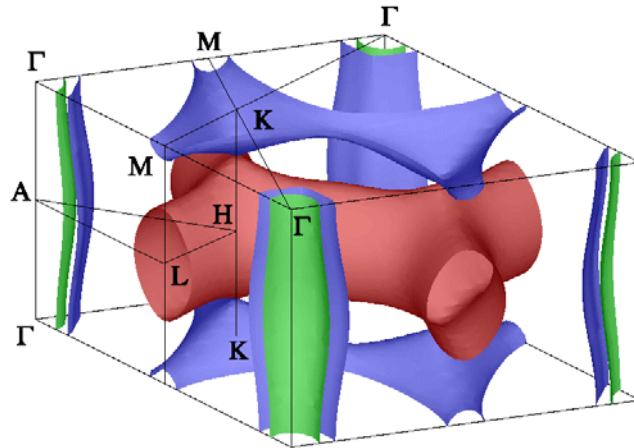


Figure 10. The Fermi surface of MgB_2 consists of two cylindrical sheets due to the σ -bands and a tubular network derived from the π -bands [43].

After several years of intense experimental and theoretical research, the main features of superconductivity in MgB_2 now seem to be well-understood within the framework of a phonon-mediated mechanism with different coupling strengths to the electronic σ - and π -bands [43, 44, 131–138], leading to the appearance of two distinct superconducting gaps. Apart from the high transition temperature of 40K, this *two-band* nature of the superconductivity in MgB_2 is a novelty which is still attracting much attention. In fact, at present it appears that MgB_2 is the only superconductor for which substantiated theoretical and experimental evidence for multi-band superconductivity exists. The multi-band superconductivity in MgB_2 has been

observed or inferred independently by several experimental techniques, such as tunneling, Raman and angle-resolved photoemission spectroscopies, heat capacity and penetration depth measurements, and the analysis of the critical fields [139]. *Ab initio* electronic structure calculations [43, 131] by several groups also point to the existence of two-band superconductivity in MgB_2 .

The Mg atom donates its two valence electrons completely to the graphenelike boron layer. There is hardly any Mg contribution to the density of states at the Fermi level. The attractive potential from the Mg^{2+} ions in the hollows between the hexagonal boron layers is felt much more strongly by a p_z -electron than by a bond-electron. As a result, the π -band is pulled down in energy, while the σ -bands remain partially filled, i.e. there are holes at the top of the σ -bands. MgB_2 has a total of 0.26 holes: 0.15 holes in the two σ -bands crossing the Fermi level and the remaining 0.11 holes in the π -band. The presence of holes on the top of the bonding σ -bands is one of the unusual, but important, features of the electronic structure of MgB_2 .

The holes in the σ -band couple strongly to the optical $B - B$ bond-stretching vibrations, and it is primarily this coupling that drives the superconductivity in MgB_2 . It has been demonstrated that the optical bond-stretching E_{2g} phonons (see Fig. 11) at the Γ point couple most strongly to the holes at the top of the σ -bands, while the three-dimensional π -electrons couple only weakly to the phonons. The E_{2g} modes are doubly-degenerate optical $B-B$ bond-stretching modes. Close to $\Gamma-A$, they have exactly the same symmetry and similar dispersions as the light and heavy σ -hole bands.

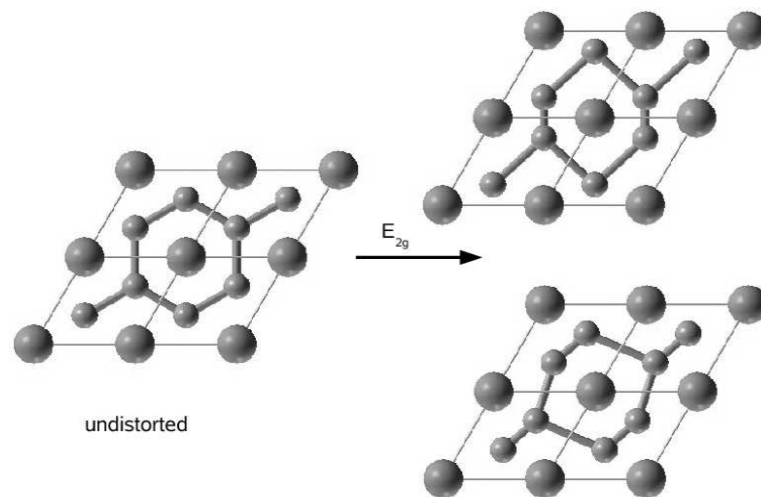


Figure 11. The E_{2g} phonon mode in MgB_2 is a doubly-degenerate Raman active optical mode, where two of the $B-B$ bonds are stretched or compressed. The right side shows the displacement of the atoms in the unit cell for the so-called x - and y -polarization. The left side is a representation of the undistorted MgB_2 crystal for comparison.

The different coupling strengths of the σ - and π -bands lead to superconducting gaps different in character and size [44, 132–135]. Using linear response theory, it is possible to calculate the electron-phonon coupling and Eliashberg functions from first principles. Kong *et al.* used the FP-LMTO linear response code of Savrasov to compute the phonon properties and the Eliashberg function for MgB₂, as shown in Fig. 12. One striking feature is that, unlike in most other cases, the shape of the Eliashberg function with respect to frequency does not follow the phonon DOS. An anomalously large coupling of the E_{2g} phonon branch along the Γ –A direction gives rise to a peak around the 530 cm⁻¹ region, dwarfing contributions from all other phonons (Fig. 12). The E_{2g} optical phonon frequency at the Γ point is 532 cm⁻¹.

Various physical properties of the superconducting state can be calculated from the Eliashberg spectral and transport functions. The superconducting gaps for clean MgB₂ obtained from the Eliashberg theory are in very good agreement with experiments [136, 140]. The Eliashberg functions calculated by Kong *et al.* [132] have further been used successfully to describe the specific heat [140], tunneling [141], penetration depth [142] and thermodynamic properties [143].

The two-band aspect of the superconductivity in MgB₂ can be observed only if the effect of interband scattering by impurities between σ - and π -bands is very small. The importance of the role of impurities in the observed properties of MgB₂ was noted as early as 2002 [144], and since then, this particular issue has become one of the main research topics in the field. As for any anisotropic order parameter, scattering by nonmagnetic impurities should have a pair breaking effect. Interband impurity scattering should lead to a decrease

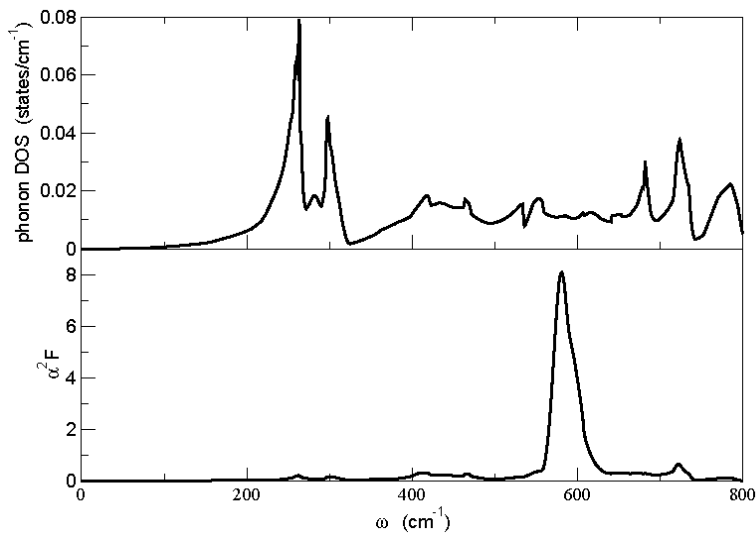


Figure 12. FP-LMTO linear response results for the phonon dispersion $F(\omega)$ and the Eliashberg spectral function $\alpha^2 F(\omega)$ for MgB₂.

of T_c and, if strong enough, to a single or averaged order parameter [145], as given by Eq. (5). The interband impurity scattering between the σ - and π -bands is exceptionally small, due to the particular electronic structure of MgB_2 [146], so that in the superconducting state the two gaps in the σ - and the π -bands are preserved even in 'dirty' samples with reduced T_c 's and a broad range of normal state resistivities. It should be noted that a proper treatment [147] of nonmagnetic impurity scattering using the Eliashberg theory for the two-band model yields a much slower rate of T_c suppression with impurity concentration, compared with the prediction based on the BCS theory. Such a treatment also produces results in excellent agreement with experiments. The BCS treatment ignores renormalization and damping associated with the electron-phonon interaction. Erwin and Mazin [148] have considered the effects of lattice distortion by various impurities and their influence on scattering, stimulating experimental groups worldwide to check the predictions.

The decrease of T_c has been demonstrated by a series of experiments in which Mg has been substituted by considerable fractions of Al and B by C. It has been observed that the σ gap decreases with decreasing T_c and approaches an intermediate coupling value of $2\Delta/k_B T_c$ at $T_c \sim 25$ K. In most experimental reports the π gap is found to be independent of the T_c of the sample with a value close to ~ 2 meV, as seen for undoped samples. This remained a mystery for a while, as it appeared not to be in agreement with the otherwise successful theory of two band superconductivity of MgB_2 , which predicts a merging of the two gaps. This behaviour can be explained by considering the effect of band filling by impurities together with the effect of interband scattering [149]. More details on the influence of doping on the properties of MgB_2 are given elsewhere [150].

Since most of the EP coupling in MgB_2 arises from the coupling of a few zone center σ -holes to the E_{2g} optical phonons, a reasonably good estimate of the EP coupling constant λ can be obtained from a result which relates the EP matrix element for an optic mode to the corresponding deformation potential. On the basis of this result, first derived by Khan and Allen [151], the EP coupling parameter for the two degenerate zone-center E_{2g} modes can be written as [131]:

$$\lambda \sim \lambda_{E_{2g}} = \frac{N_\sigma(0)D^2}{M\omega^2}, \quad (22)$$

where $N_\sigma(0)$ is the density of σ states per spin at the Fermi level, M is the B - B reduced mass participating in the optical bond-stretching phonon, and $\pm Du$ is the energy splitting of the doubly-degenerate top of the σ -band produced by

the displacement $\mathbf{e}u$ of the same bond-stretching phonon, with normalized eigenvector \mathbf{e} (see Fig.3 of [131]). There is a feedback effect between λ and the phonon frequency: the optical phonons are softened by the interaction with the σ -holes. ω is renormalized with respect to its *bare* value ω_0 due to the EP coupling according to $\omega^2 = \omega_0^2/(1 + 2\lambda)$, and this, in turn and according to Eq.(22), enhances λ .

Eq.(22) can be considered as the Hopfield formula for an optical phonon. In the following discussions, Eq.(22) will be useful in comparing the EP coupling and superconducting properties of MgB_2 with those of Boron-doped diamond and other superconductors with a layered MgB_2 -type structure.

3.4. Boron-doped diamond: Similarities and differences with respect to MgB_2

The transparent diamond is a typical band insulator. Thus it came as quite a surprise, when it was shown that under extremely high boron doping (*e.g.* 3 %) diamond undergoes a superconducting transition with a critical temperature of 4 K [152]. Such high hole-doping levels can be achieved due to the small size of boron. It had previously been observed that the prominent Raman line caused by the zone-center optical phonons at 1332 cm^{-1} downshifts and broadens significantly upon heavy boron doping [153]. After the initial report in polycrystalline samples, the result has also been confirmed in thin films, with T_c 's as high as 11 K.

Besides creating an obvious technological interest, as diamond is a promising material for application in electronics, these findings posed fundamental questions concerning the superconducting mechanism and the possibility of observing superconductivity in other doped semiconductors.

At these high doping concentrations, which are one order of magnitude larger than those at which an insulator-metal transition takes place, B-doped diamond can be described as a degenerate metal. This allows us to apply the standard linear-response method to calculate the phonon spectrum and electron-phonon coupling. These calculations not only show that electron-phonon coupling is the most likely explanation for the observed superconductivity, but also reveal an unexpected similarity between hole-doped diamond and MgB_2 .

To model the effect of doping, one can use the Virtual Crystal Approximation (VCA): the real solid is approximated by a solid of virtual atoms with charge $Z_{\text{virt}} = (1-x)Z_C + xZ_B$, where x is the fraction of carbon atoms replaced by boron. This allows for a relatively straight-forward way of studying the electronic structure and the physical properties of hole-doped diamond for different doping levels x . This simple approximation captures a

lot of the essential physics. One should, however, expect a more qualitative explanation of the mechanism rather than quantitative agreement. In fact, several important new features, such as the appearance of new phonon modes due to boron, are completely neglected.

Even at $x = 0.1$, the band structure of hole-doped diamond is still almost identical to that of pure diamond: the 4 sp^3 hybrids on each C atom form 4 bonding (valence) and 4 anti-bonding (conduction) bands, separated by a large gap. The exceptional hardness of diamond derives from the fact that the only states which are full are all of σ -bonding character, and these form bonds which are among the strongest in nature. With boron doping, electrons are removed from the crystal and holes form at the top of the triply-degenerate valence band. Diamond becomes metallic, with the holes forming three distorted spherical Fermi surfaces around the center of the Brillouin zone [154]. The average radius of the spheroids grows with doping as $k_F \simeq \left(\frac{x}{3}\right)^{1/3} k_{\text{BZ}}$; the density of states (DOS) has a typical 3d behaviour, and its value at the Fermi level, $N(\varepsilon_F)$, grows as $x^{2/3}$.

The effect of doping on the phonon spectrum is shown in Fig. 13. There is a sizeable reduction (softening) of the frequency of the zone-center optical phonon with increasing doping level x . The softening increases and extends to a larger region in q -space, which can be understood in terms of the standard electron-phonon theory. In metals, the interaction of conduction electrons with a phonon causes a reduction of its frequency, which grows with the strength of

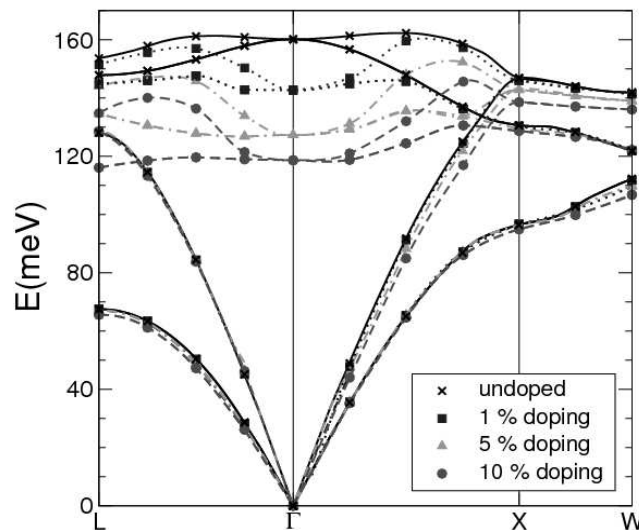


Figure 13. Phonon dispersion of pure and hole-doped diamond for different values of boron concentration x . There is a pronounced softening of the frequency of the zone-center optical phonon with respect to the pure case, which increases as a function of x . Figure from Ref. [155].

the interaction. Further, theory shows that only phonons with $q < 2k_F$ are allowed to couple. Fig. 13 thus shows that only the optical modes around Γ couple with increasing strength with doping. A simple physical picture explains why in this material electrons couple strongly to some lattice vibrations. The optical phonon, which at the zone-center has the same symmetry as the electronic states at the top of the valence band, is a bond-stretching mode which distorts the stiff σ -bonds. In fact, when the ions are moved along the eigenvector of the Γ optical mode, the triple degeneracy of the top of the σ -band at the Γ point is removed, with one band moving to lower and one to higher energies, while the third band remains fixed (see Fig. 1 in Ref. [155]). The splitting of the bands can be directly related to the strength of the deformation potential, and to the EP coupling parameter via Eq.(22).

The nature of EP coupling in diamond is very similar to that in MgB_2 , with a few differences due to dimensionality. In fact, MgB_2 is a layered material quite similar to graphite, the 2D form of carbon, which, unlike diamond, is based on sp^2 bonding. Instead of four σ -bands, there are three σ - and one π -band. The top of the σ -band, which contains the superconducting holes, is doubly-degenerate, with the same symmetry as the bond-stretching E_{2g} phonon mode. In MgB_2 , all the σ electrons couple to each of the degenerate phonon vibrations, whereas in diamond only 2 bands out of 3 are coupled to each of these phonons. The Hopfield formula, Eq.(22), shows that the total electron-phonon coupling is determined by material-dependent parameters, such as the density of states at the Fermi level, the deformation potential, and the characteristic phonon frequency ω . Due to the EP coupling, the latter is softened with respect to its bare value ω_0 , the value without any coupling between the phonons and the electrons. The interplay between λ and ω can be captured by introducing a bare electron-phonon coupling $\lambda_0 = \frac{N(\epsilon_F)D^2}{M\omega_0^2}$. The bare

phonon frequency ω_0 is a measure of the hardness of the material. D is a measure of the distortion of the electronic bands due to phonons. λ_0 is the EP coupling constant the material would have, if the phonon frequencies were not influenced by the EP coupling. As mentioned earlier, there is a feedback effect between the EP coupling and phonon frequency. This feedback effect is similar between MgB_2 and hole-doped diamond, except for one difference. In MgB_2 , the phonon frequency renormalization is given by $\omega^2 = \omega_0^2 / (1+2\lambda)$, as the holes in each of the two degenerate σ -bands couple to the zone center $B - B$ optical phonons. In diamond, only 2 bands out of 3 σ -bands couple to the zone-center optical phonons, modifying the above relation as $\omega^2 = \omega_0^2 / \left(1+2\left(\frac{2}{3}\right)\lambda\right)$. Thus, the difference between the renormalization of the EP coupling constant λ with

respect to its bare value λ_0 in these two systems can be captured in a single relation: $\lambda = \frac{\lambda_0}{1-2\alpha\lambda_0}$, with $\alpha = 1$ in 2D (MgB₂) and $2/3$ in 3D (hole-doped diamond).

Values of several quantities for boron-doped diamond at different levels of boron-doping and the same for isostructural Si and Ge are given in Table 3. Even though at $x = 0.1$ diamond has the same λ_0 as MgB₂ due to the compensating effects of a larger deformation potential and phonon frequency, its effective electron-phonon coupling parameter λ is much lower (0.6 instead of 1.0). This reduction is entirely due to dimensionality effects, represented by the factor α . The value of λ in diamond grows on doping, following the increase of $N(\varepsilon_F)$.

In the same table, the value of λ_0 , obtained by the numerical integration of the total Eliashberg function $\alpha^2F(\omega)$, evaluated on a very fine $(1/12)^3$ grid in q -space, is also reported (λ_{num}). In diamond, the agreement between the approximate Hopfield formula and the numerical result, which takes into account the full complexity of the electronic and vibrational spectrum, is striking. In fact, the shape of the Eliashberg function indicates that the electron-phonon coupling is actually concentrated in the bond-stretching phonon branch.

In the case of the other tetrahedral semiconductors Si and Ge, their bare and total electron-phonon coupling parameters are always lower than the corresponding ones of diamond. This is mainly due to the deformation potentials which are lower. Furthermore, in these cases, the agreement between the Hopfield formula and the numerical estimate of λ is somewhat poorer, as the Eliashberg function shows that other phonon branches are involved in the coupling.

Table 3. Values of the parameters which determine the total electron-phonon coupling λ according to the Hopfield formula (22). $N(\varepsilon_F)$ is in states/eV/spin/f.u., D is in eV/Å and ω in cm^{-1} . The total electron-phonon coupling, obtained by the numerical integration of the full Eliashberg function (λ_{num}), is also reported.

	$N(\varepsilon_F)$	D	ω	λ_0	λ	λ_{num}
MgB ₂	0.15	12.4	536	0.33	1.01	1.02
C	0.00	21.6	1292	0	0	0
3%C	0.07	21.1	1077	0.21	0.30	0.30
5%C	0.08	20.8	1027	0.25	0.37	0.36
10%C	0.11	20.4	957	0.32	0.57	0.56
Si	0.00	6.8	510	0	0	0
5%Si	0.17	6.3	453	0.13	0.16	0.30
10%Si	0.24	6.1	438	0.17	0.22	0.40
Ge	0.00	5.8	317	0	0	0
10%Ge	0.20	4.4	282	0.08	0.09	0.32

The Eliashberg function can also be obtained from experiment. In case of boron-doped diamond, this has been achieved, using coherent synchrotron radiation measuring the reflectivity of thin films. The theoretical predictions show that most of the electron-phonon interaction is provided by the optical phonon branch around 1200 cm^{-1} . The agreement between theory and experiment [156] is particularly impressive in the calculation of Ref. [157], which includes the effect of distortion of the diamond lattice due to boron impurities. Correspondingly, new boron modes appear at lower energies, which also provide part of the electron-phonon coupling.

3.5. Superconductivity in MgB_2 -type hexagonal layered compounds

3.5.1. The Diborides XB_2 , $\text{X}=\text{Mg}, \text{Ca}, \text{Be}$

Since the discovery of superconductivity in MgB_2 , interest in metallic as well as potentially metallic layered compounds has grown in the context of the search for systems with higher T_c . From this standpoint, systems of immediate interest are other diborides, where the Mg sublattice is wholly or partially replaced by other divalent elements, such as Be, Ca, Sr, etc. A considerable amount of both theoretical and experimental work has already been carried out in this regard, without any spectacular success so far [133, 158–162]. Calculations involving MgB_2 -based ternary borides ($\text{MgB}_{2-y}\text{X}_y$, $\text{X}=\text{Be}, \text{C}, \text{N}, \text{O}$) show that electron-doping of the B sublattice is counterproductive to superconductivity [158], while hole-doping of the Mg sublattice, though promising, has not been found very effective either [158]. For pedagogical reasons, we will undertake a comparative study of three diborides: MgB_2 , CaB_2 and BeB_2 . The band structure of the three diborides in the $P6_3/mmm$ structure is shown in Fig. 14. The energy bands shown were computed using the LMTO-ASA method, and they are virtually identical to the bands obtained via the FP-LMTO scheme. For MgB_2 , we have used

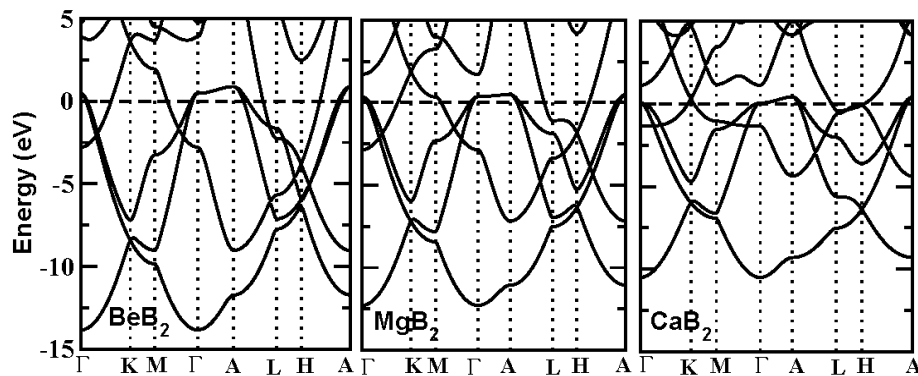


Figure 14. LMTO-ASA energy bands for the three compounds: MgB_2 , BeB_2 and CaB_2 , all in the $P6_3/mmm$ structure.

experimental values of c and a [163]. For CaB_2 and BeB_2 , we use the same c/a ratio as in Ref. [162]. However, the lattice parameter a was varied to obtain minimum energy using LMTO-ASA. Therefore, these values are somewhat different from those used in Ref. [162] (1% higher for BeB_2 , and 4% lower for CaB_2). The diborides MgB_2 , BeB_2 and CaB_2 are metallic via self-doping, and their energy bands, as seen in Fig. 14, are very similar.

As discussed in section 3.3, the bulk of EP coupling in the diborides should arise from the coupling of the σ -holes to the zone center E_{2g} optical phonons. By introducing B-B bond stretching distortion in the unit cell of the diborides, it is easy to verify that the zone-center E_{2g} optical phonon splits the σ -bands close to the Fermi level into almost parallel bands. One can calculate the deformation potential D for this phonon from the magnitude of the band splitting and use the Hopfield formula, Eq.(22), to estimate the EP coupling parameter λ . As an example, the band splitting in CaB_2 due to the E_{2g} phonon is shown in Fig. 15.

Using this result and assuming that the total EP coupling parameter λ simply scales as the strength of corresponding λE_{2g} in the diborides, we can write for the ratio of EP coupling in the two diborides A and B:

$$\lambda^A/\lambda^B = \frac{N_\sigma^A D_A^2 \omega_B^2}{N_\sigma^B D_B^2 \omega_A^2}, \quad (23)$$

where the sub(super)scripts A and B refer to the two diborides.

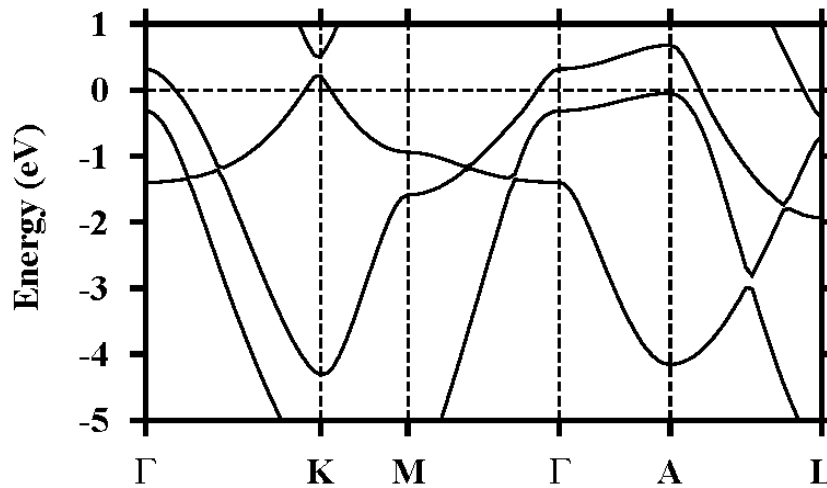


Figure 15. Band structure of CaB_2 with frozen-in E_{2g} mode corresponding to a 4% change in B-B bond length, plotted along the symmetry directions of the undistorted P_{63}/mmm structure. The E_{2g} phonon breaks the symmetry and, in this example, splits the σ -bands by about 0.8 eV along Γ -A direction.

In Table 4, the lattice parameters, deformation potentials and the σ -part of the DOS at the Fermi level are presented. The last column in Table 4 should be proportional to the Hopfield parameter η . In BeB_2 the deformation potential is slightly higher than in MgB_2 because of its smaller bond length. The smaller value of $N_\sigma(0)$ causes the Hopfield parameter for BeB_2 to be smaller than MgB_2 . The EP coupling parameter λ should be further lowered in BeB_2 , as the shorter BB bond should have a higher E_{2g} -mode frequency compared with that for MgB_2 . This conclusion is similar to that reached by Profeta *et al.* [164]. According to the current data base, the only compounds formed from the two elements B and Be are: BeB_3 (P6/mmm), Be_2B (Fm 3 m), and Be_4B (P4/MMMS) [165]. Note that the higher density of states at the Fermi level in CaB_2 , due essentially to lattice expansion, prompted several authors [43, 158, 162] to suggest that either CaB_2 or Ca-doped MgB_2 should be a likely candidate for a solid with higher T_c .

Purely for pedagogical reasons, we explore the relative changes in the charge densities in these solids, induced by the excitation of an E_{2g} phonon. In Fig. 16, we show the total charge densities along the lines joining the two boron atoms involved in the E_{2g} -mode coupling. This is a measure of the bond strength. For EP coupling, the appropriate indicator is not the total charge density, but the charge density due to the wave functions with energies in a small window around the Fermi level (henceforth, the Fermi level charge density). The inset of Fig. 16 shows the Fermi level charge density along the B-B line in MgB_2 and BeB_2 for wave functions within an energy window of 0.046 Ry around respective Fermi levels ($E_F \pm 0.023$ Ry). This quantity is higher in MgB_2 , although the total charge density is higher in BeB_2 due to shorter bond length.

The coupling of the E_{2g} -mode phonons to the electrons can be seen in the alteration of the Fermi level charge density due to the E_{2g} distortion of the unit reference compound. The McMillan equation, assuming $\mu^* = 0.1$, produces

Table 4. LMTO-ASA results for the E_{2g} -mode deformation potentials and the σ -part of the DOS at the Fermi level, $N_\sigma(0)$ (states/(eV spin f.u.)). D = deformation potential (eV/ Å). The basis consisted of s -, p -, d -, and f -orbitals on all atoms, with f -orbitals downfolded. For each compound, the lattice parameters a (in a.u.) and c/a ratio are also shown.

	a	c/a	$N_\sigma(0)$	D	$N_\sigma(0)D^2$
BeB_2	5.525	1.027	0.12	13.0	20.3
MgB_2	5.826	1.142	0.15	12.0	21.6
CaB_2	6.15	1.183	0.17	9.0	13.8

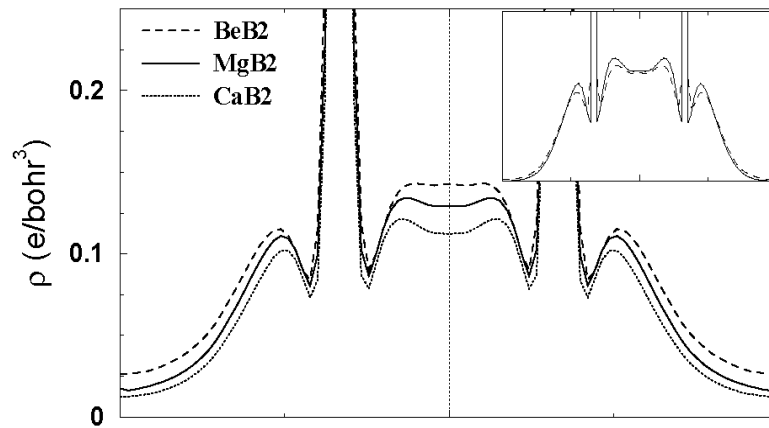


Figure 16. Total valence charge density ρ along the B-B bond in MgB_2 , BeB_2 , and CaB_2 . The inset shows the charge density from wave functions within a 0.046 Ry window around the respective Fermi levels. Though the total bond center charge density is higher in BeB_2 , that due to wave functions within the 0.046 Ry window is lower. The entire vertical axis in the inset represents a valence charge density of 0.01 e/bohr³.

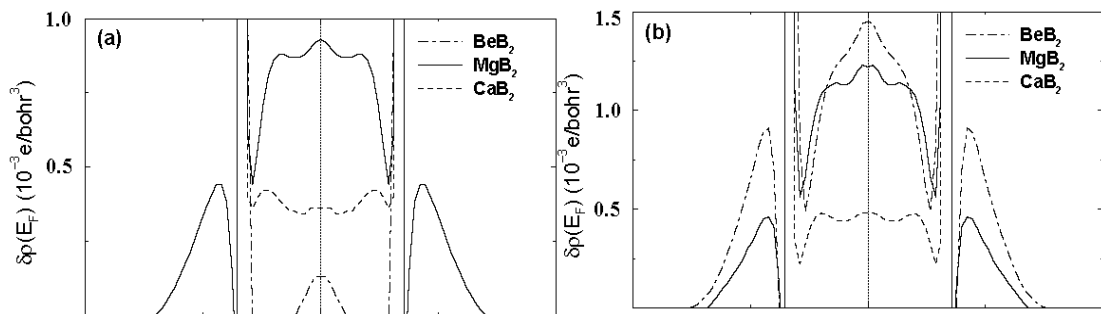


Figure 17. Alteration in Fermi level charge density $\delta\rho(E_F)$ due to the E_{2g} -mode bond stretching. The quantity plotted is a qualitative measure of the electronic part of the electron- (E_{2g}) phonon coupling (see text for details). The energy windows used are 0.046 Ry in (a) and 0.08 Ry in (b).

cell. In Fig. 17, we have plotted this quantity for the same compounds considered in Fig. 16. The energy window is 0.046 Ry in (a) and 0.08 Ry in (b). For convenience, the charge density considered is that along the line of the original (undistorted) bond, both before and after E_{2g} bond stretching is introduced. The plotted quantity is the difference in the charge density: original minus the E_{2g} stretched bond, and it can be considered as a qualitative measure of $N(0) \langle I^2 \rangle$, where $\langle I^2 \rangle$ is the average square electron-phonon(ion) matrix element, as defined by McMillan [50]. The trend revealed in Fig. 17 should qualitatively follow the trend shown in Table 4. Note that the actual values of Fermi level charge density alterations are dependent on the energy window used.

FP-LMTO linear response calculations of Kong *et al.* [132] for MgB₂ yield the Γ -point E_{2g} -mode frequency $\omega_{E_{2g}} = 585 \text{ cm}^{-1}$ and $\omega_{ln} = 481 \text{ cm}^{-1}$. The values of the E_{2g} -mode frequency for MgB₂, CaB₂ and BeB₂ in our FP-LMTO linear response calculations are 532 cm^{-1} , 335 cm^{-1} and 820 cm^{-1} , respectively. In the absence of the knowledge of ω_{ln} for CaB₂ and BeB₂, we make the simplifying assumption $\omega_{E_{2g}} = \omega_{ln}$ for all three diborides. Using $T_c = 40 \text{ K}$ and the Coulomb pseudopotential $\mu^* = 0.1$ in the Allen-Dynes form of the McMillan equation, we get the EP coupling parameter $\lambda = 0.84$ for MgB₂, in good agreement with the value obtained via full linear response calculations by different authors [44, 132]. The scaling arguments of Rosner *et al.* [166](Eq.23) yield estimates for λ in CaB₂ and BeB₂, with MgB₂ being the estimates of T_c . The results are summarized in Table 5. The estimated λ and T_c for BeB₂ are in good agreement with the results obtained by Profeta *et al.* [164].

In Table 6, we present the Γ -point E_{2g} -mode frequencies calculated for various a values and c/a ratios in MgB₂. The results for CaB₂ and BeB₂ are also

Table 5. The Γ -point E_{2g} -mode frequency from linear response calculation, EP coupling parameter based on Eq.(23) and using MgB₂ as the reference system, T_c based on the Allen-Dynes form of the McMillan formula.

	$\omega(E_{2g}) (\text{cm}^{-1})$	$\omega(E_{2g}) (\text{K})$	λ	$T_c (\text{K})$
BeB ₂	820	1180	0.34	1.7
MgB ₂	532	765	0.84	39.5
CaB ₂	335	482	1.35	49

Table 6. The Γ -point E_{2g} -mode frequency from linear response calculation, as a function of the lattice parameter.

	a	c/a	$\omega(E_{2g}) (\text{cm}^{-1})$
CaB ₂ *	6.419	1.183	285
CaB ₂	6.150	1.183	336
MgB ₂	6.014	1.163	391
MgB ₂	6.014	1.142	396
MgB ₂	6.014	1.120	409
MgB ₂	5.925	1.142	472
MgB ₂	5.925	1.120	484
MgB ₂	5.826	1.142	532
MgB ₂	5.727	1.142	610
MgB ₂	5.575	1.102	749
BeB ₂	5.525	1.027	820

*see [167] for clarification.

included to examine possible universal (smooth) dependence of the frequency of this mode as a function of the lattice parameter, irrespective of the atom type in the Mg sublattice. The results presented in Table 6 are plotted in Fig. 18, for different choices of the c/a ratio in some cases, to emphasize the observation that the dependence of $\omega(E_{2g})$ on the lattice parameter (volume) in these hexagonal structures does indeed bear out to be smooth, providing a guidance toward engineering materials with preselected T_c . Of course, the issue of stability of these compounds and the stability at particular volumes is of paramount importance. The compound CaB_2 may not be stable. However, the results suggest that partial doping of the Mg sublattice by Ca in MgB_2 may lead to higher T_c . Medvedeva *et al.* [158] have suggested creating layered superstructures of the $\text{MgB}_2/\text{CaB}_2$ type in search of higher T_c . In SrB_2 , the Fermi level seems to fall in a pseudogap [162], which indicates high stability for this compound. However, reduced density of states at the Fermi level due to the pseudogap also points to lower EP coupling, thus suggesting that SrB_2 is not a likely candidate for a higher T_c superconductor.

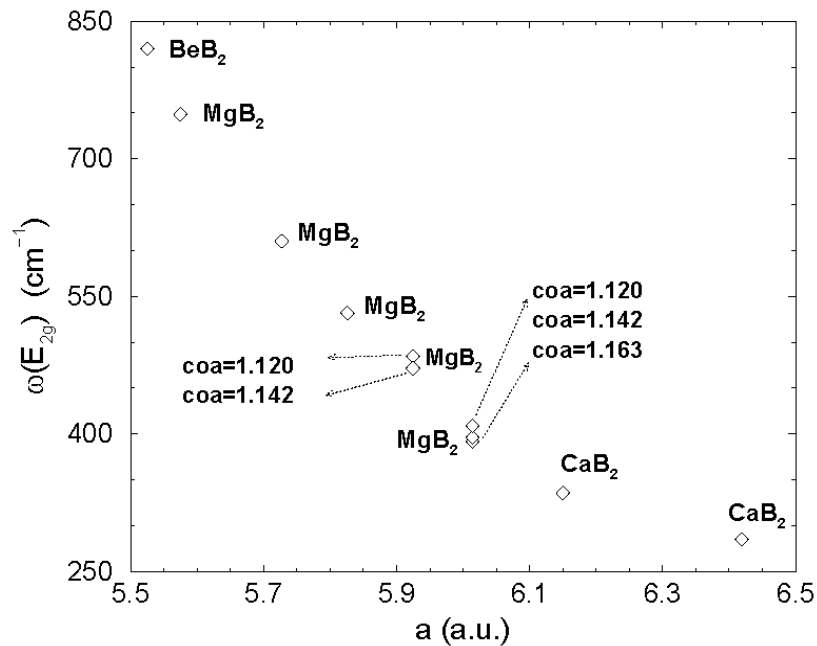


Figure 18. Variation of $\omega(E_{2g})$ with the lattice parameter a in MgB_2 -type compounds ($\text{coa} \equiv c/a$).

3.5.2. Hexagonal ternary compounds in $P6_3/mmm$ structure: LiBC, LiBeN, MgBeC

For comparison with the diborides, we study three ternary compounds (hole-doped): LiBC, LiBeN, and MgBeC, all in $P6_3/mmm$ (No.194) structure with A-B stacking. The case for hole-doped LiBC was first advanced by

Pickett and co-workers [166] as a promising candidate for a high T_c solid, a conclusion based on virtual crystal calculation of electronic structure and the scaling arguments embodied in Eq.(23). This was later retracted with plausibility arguments as to why the expectations based on simple scaling arguments and perhaps also linear EP coupling theory cannot be met [168] for solids such as hole-doped LiBC. The concerns regarding such inadequacies also apply to some extent to MgB_2 . To date, LiBC has not been found to be superconducting for any level of hole-doping. However, it does serve as a case for us to understand some of the limitations of the present state of the theory of phonon-mediated superconductivity.

LiBC is isostructural and isovalent with MgB_2 , with graphene-like B-C layers that are more strongly bonded than the B layers in MgB_2 . LiBC is a stable compound and, in its stoichiometric form, is semiconducting [169]. Li deficiency can render it metallic by introducing carriers (holes) in the B-C σ -bands, as occurs naturally in MgB_2 . Calculations based on virtual crystal approximation to simulate hole-doping or Li deficiency (i.e. by reducing the valence charge of Li) show a rigid band behaviour as a function of hole-doping, making this an ideal system to study the variation in the strength of EP coupling as a function of Li deficiency. As discussed below, independent calculations by us and the scaling arguments based on Eq.(23) do yield a large value of EP coupling and very high T_c for hole-doped LiBC.

The B-C bond is stronger than the B-B one, although more ionic in character. In general, more ionic bonds are also softer. This may result in a smaller deformation potential, but also in a lower frequency for the bond stretching mode. It is thus not clear *a priori* whether layered compounds with more ionic intralayer bonds will have stronger/weaker EP coupling. Motivated by this consideration, we have selected the above three isoelectronic compounds, LiBC, LiBeN, and MgBeC, with different perceived intralayer bond strengths. While diborides such as MgB_2 , BeB_2 and CaB_2 are metallic (via self-doping), the ternary compounds we have chosen are insulating/ semiconducting and, as will be clear from the band structures shown, can be rendered metallic only via hole-doping. Since it is only the σ -electrons that couple strongly to the bond stretching mode [43, 131, 132], it would be desirable to have a compound where hole-doping brings the σ -bands up to the Fermi level, while the π -bands stay lower in energy. In this respect, both LiBeN and MgBeC seem to have a definite advantage with respect to LiBC (see Fig. 19, Table 7, and related discussion). Both LiBeN and MgBeC in $P6_3/mmc$ structure are hypothetical, but the object here is to explore whether there may be some motivation to stabilize them in this structure.

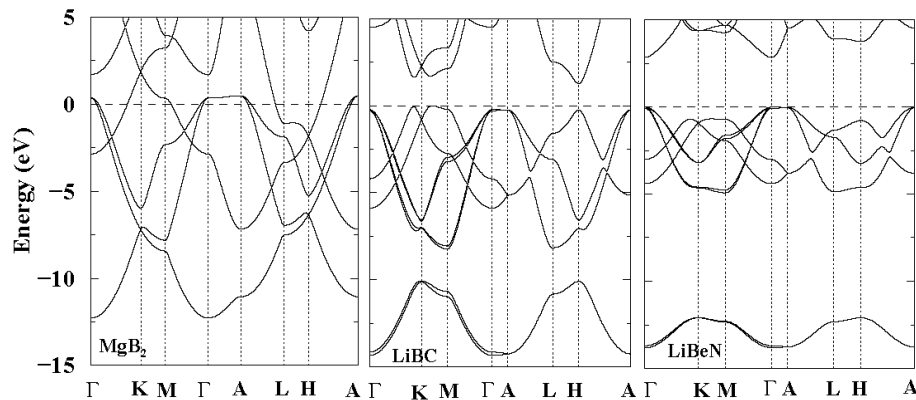


Figure 19. LMTO-ASA energy bands for the three compounds: MgB_2 ($P6_3/mmm$), LiBC ($P6_3/mmc$), and LiBeN ($P6_3/mmc$).

Table 7. LMTO-ASA results for the E_{2g} -mode deformation potentials and the σ -part of the DOS at the Fermi level, $N_\sigma(0)$ (states/(eV spin f.u.)). D = deformation potential (eV/Å). The basis consisted of s -, p -, d -, and f -orbitals on all atoms, with f -orbitals downfolded. For each compound, the lattice parameters a (in a.u) and c/a ratio are also shown.

	a	c/a	$N_\sigma(0)$	D	$N_\sigma(0)D^2$
MgB_2	5.826	1.142	0.15	12.0	21.6
$\text{Li}_{0.5}\text{BC}$	5.201	2.564	0.15	18.0	48.6
$\text{Li}_{0.5}\text{BeN}$	5.5	2.6	0.30	9.0	24.3
$\text{Mg}_{0.5}\text{BeC}$	6.200	2.000	0.37	6.0	13.3

For LiBC , we use experimental values of the lattice parameters c and a [169]. For the hypothetical compounds, we use energy-optimized values of c and a , either from previous publications [160, 162], or by using LMTO-ASA. Since the results presented are of pedagogical interest only, serving to illustrate the dependence of the deformation potential on the intralayer (nearest neighbour) bond length and the degree of ionicity, the lattice parameters were adjusted to get reasonably close to the energy minimum, but the c and a values used were not the *exact* minimum energy values. In Fig. 19, we compare the LMTO-ASA bands for the three compounds: MgB_2 , LiBC , and LiBeN .

In Fig. 20, we show the energy bands in LiBC and LiBeN to illustrate the advantage of LiBeN over LiBC : it is possible to hole-dope (up to at least 17%) the σ -bands of LiBeN without doping into the π -bands, while in LiBC both σ - and π -bands get doped simultaneously. The compound MgBeC has a similar advantage over LiBC . Both LMTO-ASA and FP-LMTO calculations for undoped LiBC show the π -bands touching the Fermi level, while the

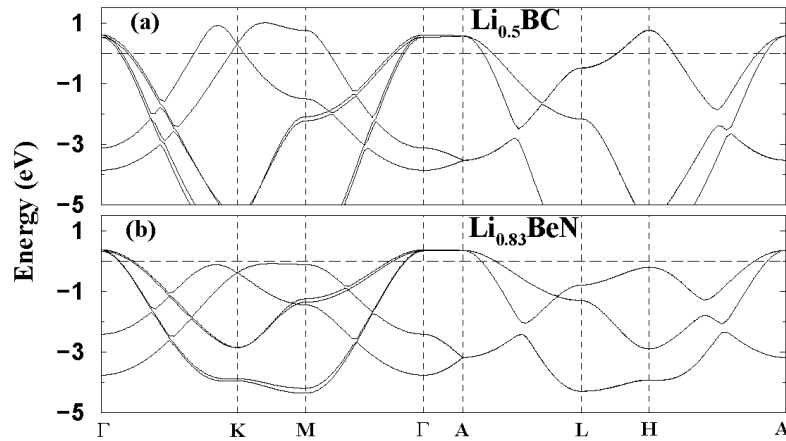


Figure 20. FP-LMTO band structures of (a) $\text{Li}_{0.5}\text{BC}$ and (b) $\text{Li}_{0.83}\text{BeN}$. Without hole-doping both compounds are insulators. With hole-doping the bands move rigidly upward (with respect to the Fermi level). In case of LiBC, it is not possible to hole-dope into the σ -bands without doping into the π -bands. Both LMTO-ASA and FP-LMTO calculations for undoped LiBC show the π -bands touching the Fermi level, while the σ -bands remain slightly below (contrary to Fig.2(a) of Ref. [166]). For LiBeN, about 20 % hole-doping is possible without doping into the π -bands.

σ -bands remain slightly below (contrary to Fig.2(a) of Ref. [166]). In LMTO-ASA, it is necessary to include the f -states in the basis for all the atoms (although they can be downfolded) to obtain this result.

In Table 7, we show the E_{2g} -mode deformation potentials and the σ -part of the DOS at the Fermi level, $N_{\sigma}(0)$, for the various compounds. While $N_{\sigma}(0)$ depends on the shape of the σ -bands at the Fermi level, the deformation potential depends on the nearest neighbour intralayer distance and the covalency(ionicity) of the bond. As in the case of the diborides, we calculate the deformation potential from the σ -band splitting due to a frozen-in E_{2g} phonon along the Γ -A symmetry direction. The σ -band splitting for $\text{Li}_{0.5}\text{BeN}$ is shown in Fig. 21.

The last column in Table 7 should be proportional to the Hopfield parameter η . It is clear that $\text{Li}_{0.5}\text{BC}$, with its high deformation potential and $N_{\sigma}(0)$ similar to that in MgB_2 , has a much stronger Hopfield parameter $\eta = N(0) \langle I^2 \rangle$, the electronic part of the EP coupling. The hypothetical compound LiBeN, despite its high value of $N_{\sigma}(0)$, ends up with a much smaller η , because of the softness (ionicity) of the Be-N bond compared with the B-C bond. If the parameters c and a for LiBeN are chosen to be the same as in LiBC, the deformation potential increases from 9.0 eV/Å to 10.3 eV/Å, which is still far smaller than the values for either $\text{Li}_{0.5}\text{BC}$ or MgB_2 . Between $\text{Li}_{0.5}\text{BC}$ and MgB_2 , the former has a larger deformation potential not just due to a shorter bond length, but (primarily) due to greater bond strength. By making

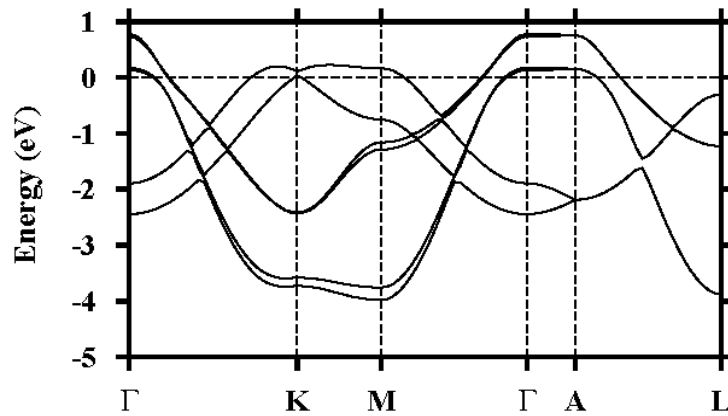


Figure 21. Band structure of $\text{Li}_{0.5}\text{BeN}$ with frozen-in E_{2g} mode corresponding to a 4% change in the Be-N bond length, plotted along the symmetry directions of the undistorted $\text{Li}_{0.5}\text{BeN}$. The E_{2g} phonon breaks the symmetry and splits the four-fold degenerate σ -bands into two doubly-degenerate ones by about 0.8 eV along the Γ -A direction.

the bond length a in MgB_2 the same as that in LiBC (keeping the c/a ratio unchanged, i.e. 1.142), we get a deformation potential of 15.3 eV/Å in MgB_2 , still smaller than the value 18.4 eV/Å obtained for LiBC . The last column in Table 7 suggests that the case for $\text{Mg}_{0.5}\text{BeC}$ may not be worth pursuing, while stabilizing hexagonal $\text{Li}_{0.5}\text{BeN}$ may still be of some interest.

As was done for the diborides, in Fig. 22 we show, for pedagogical purposes, the total charge densities along the lines joining the two atoms involved in the E_{2g} -mode coupling, a measure of the respective bond strengths. The covalent (for MgB_2) and ionic (for LiBeN and LiBC) nature of the bonds can be clearly seen. At the bond center the charge density in LiBC is much higher than in all the other compounds, despite the ionic character of the bond. This is due both to small ionicity and relatively short B-C bond length. In LiBeN , the charge density at the bond center is low, because of the increased ionicity and larger bond length. Even if the c and a parameters for LiBeN were to be the same as in LiBC , the bond center charge density would increase only by 17%, and remain much lower than that in LiBC .

The coupling of the E_{2g} -mode phonons to the electrons can be seen in the alteration of the Fermi level charge density due to the E_{2g} distortion of the unit cell. In Fig. 23, we have plotted this quantity for the same compounds considered in Fig. 22. The energy window is 0.046 Ry in all cases. For convenience, the charge density considered is that along the line of the original (undistorted) bond, both before and after the E_{2g} bond stretching is introduced. The plotted quantity is the difference in the charge density: original minus the E_{2g} stretched bond, and it can be considered as a qualitative measure of $N(0) \langle I^2 \rangle$, where $\langle I^2 \rangle$ is the average square electron-phonon (ion)

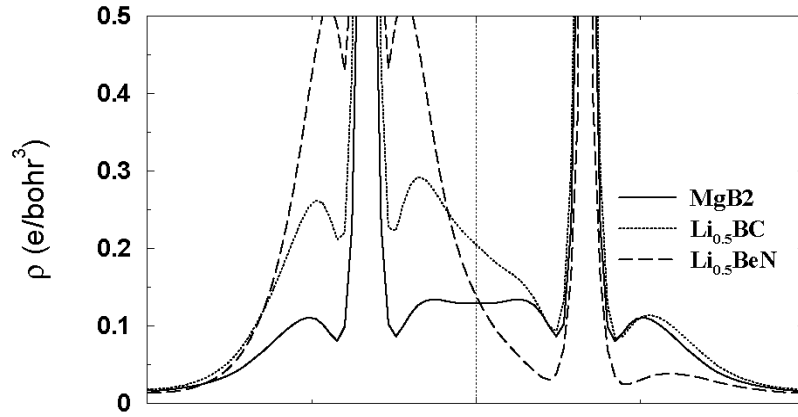


Figure 22. Total valence charge density ρ along the lines of the B-B, B-C and Be-N bonds in MgB_2 , LiBC , and LiBeN .

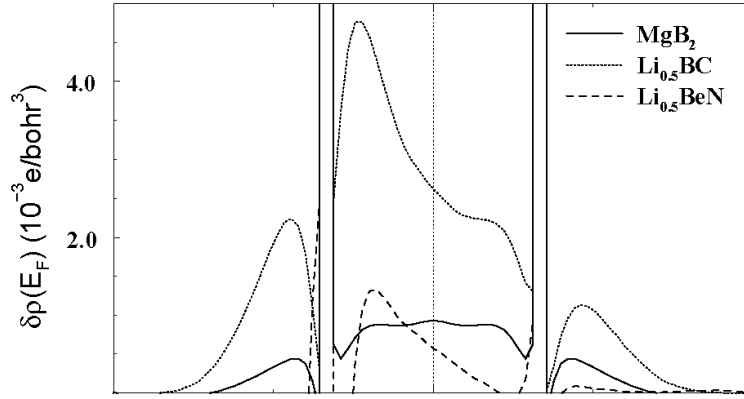


Figure 23. Alteration in Fermi level charge density $\delta\rho(E_F)$ due to E_{2g} -mode bond stretching. The quantity plotted is a qualitative measure of the electronic part of the electron- (E_{2g}) phonon coupling (see text for details).

matrix element, as defined by McMillan [50]. The trend revealed in Fig. 23 should qualitatively follow the trend shown in Table 7. The actual values of Fermi level charge density alterations are of course dependent on the energy window used.

Both deformation potential and charge density analysis reveal a very strong Hopfield parameter for hole-doped LiBC . The remaining issues are the stability of the doped compound and the frequency spectrum needed to determine the EP coupling parameter λ . We have calculated the frequency spectrum and the Eliashberg spectral function of the two compounds, $\text{Li}_{0.5}\text{BC}$ and $\text{Li}_{0.5}\text{BeN}$, using the linear response code of Savrasov [12, 13]. Virtual crystal approximation was used to simulate hole-doping. Thus, our calculations are along the same lines as followed by Pickett and co-workers [168] for $\text{Li}_{0.75}\text{BC}$ or 25% hole-doping. Our results for $\text{Li}_{0.5}\text{BC}$ or 50%

hole-doping are consistent with those obtained by these authors. For LiBeN, the Γ -point E_{2g} mode (Be-N bond stretching) comes out quite high (760 cm^{-1} for 17% hole-doping and 665 cm^{-1} for 50% hole-doping). The Brillouin zone (BZ) integrals for the dynamical matrix were carried out for a coarse mesh ((8,8,4) reciprocal lattice division). By increasing the mesh size to (32,32,16), the Γ -point E_{2g} -mode frequencies could be brought down to saturation values that are 2% lower. However, these are still high enough, so that the parameter λ actually comes out slightly lower than the value in MgB_2 , despite the larger value of $N_\alpha(0)$ (see Table 8). Besides, some low wave vectors along the Γ -A direction have imaginary (small magnitude) values (see Fig. 25). The eigenfunctions corresponding to these modes indicate a buckling tendency for the Be-N planes. LiBeN actually exists in monoclinic, $P21/c$ (No. 14), structure [170]. It can be considered as a layered compound with buckled planes, but the topology of the structure is different from that of MgB_2 -type compounds. Electronic structure calculations for LiBeN in the $P21/c$ structure provide no indication of a strong EP coupling.

For $\text{Li}_{0.5}\text{BC}$ (Fig. 24), the frequencies calculated for 30 phonon wave vectors (corresponding to a (8,8,4) reciprocal lattice division) were all positive. The frequency at a small phonon wave vector along the Γ -A direction was found to be imaginary for a coarse mesh (8,8,4) reciprocal lattice division) BZ integration for the dynamical matrix. Increasing the mesh size (to (32,32,16) reciprocal lattice division) resulted in a positive frequency. The BZ sums for the Γ point and the wave vector between Γ and A were done for a (32,32,16) mesh. For all other wave vectors the mesh size for the dynamical matrix calculation was (8,8,4). The (8,8,4) reciprocal lattice divisions do not generate any wave vectors between Γ and K points, or between A and H. A (6,6,6) reciprocal lattice division was used to generate a few of these points. The frequencies for these wave vectors are also shown, with corresponding BZ sums for the dynamical matrix performed for a (6,6,6) reciprocal lattice division. The Γ point E_{2g} -mode frequencies for undoped and

Table 8. The Γ -point E_{2g} -mode frequency from linear response calculation, EP coupling parameter based on the scaling arguments of Rosner *et al.* [166] and using MgB_2 as the reference system, T_c based on the Allen-Dynes form of the McMillan formula.

	$\omega(E_{2g}) \text{ (cm}^{-1}\text{)}$	$\omega(E_{2g}) \text{ (K)}$	λ	$T_c \text{ (K)}$
MgB_2	532	765	0.84	39.5
$\text{Li}_{0.5}\text{BC}$	712	1025	1.0	71.0
$\text{Li}_{0.5}\text{BeB}$	654	942	0.6	21.0

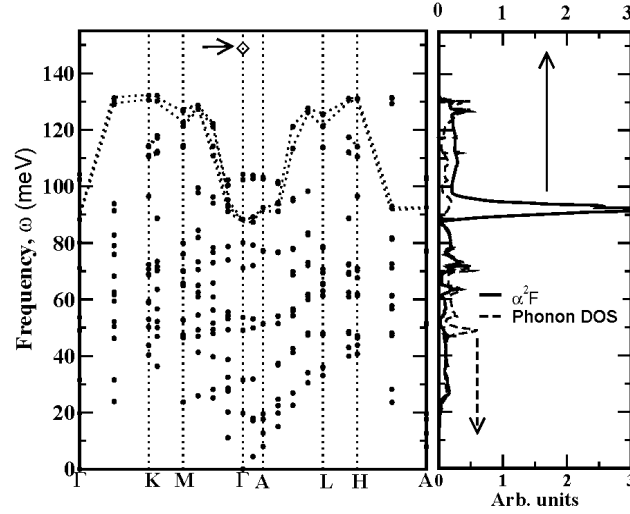


Figure 24. Phonon frequencies and DOS, and the Eliashberg spectral function for $\text{Li}_{0.5}\text{BC}$. The dotted lines show the softening of the E_{2g} phonon branch due to strong EP coupling. The E_{2g} mode is four-fold degenerate at the Γ point. The dotted lines are drawn by following the group of these four frequencies, which split into two doubly-degenerate branches. Numerical errors cause small splitting of these doubly-degenerate branches away from the symmetry points. The Γ point E_{2g} -mode frequency for the undoped compound, in excellent agreement with the value obtained by Pronin *et al.* [171] in an experimental study of the optical properties of LiBC , is shown with a diamond symbol and is also indicated with an arrow.

50% hole-doped cases are 1200 cm^{-1} (149 meV) and 712 cm^{-1} (88 meV), respectively. Our value for the undoped case agrees exactly with that of An *et al.* [168]. Note that this value $\sim 150 \text{ eV}$ for the frequency of the B-C bond stretching mode has been verified in the experimental study of the optical properties of LiBC [171] by Pronin *et al.* An *et al.* [168] also report the results for the 25% hole-doped case ($\text{Li}_{0.75}\text{BC}$). The Γ point E_{2g} -mode frequency for $\text{Li}_{0.75}\text{BC}$ in their calculation is 84 meV, consistent with our results for $\text{Li}_{0.5}\text{BC}$. Phonon frequencies calculated similarly for $\text{Li}_{0.5}\text{BeN}$ are shown in Fig. 25.

The calculated Γ -point E_{2g} -mode frequency shows some dependence on the \mathbf{k} -mesh used in the BZ integrations involved in calculating the dynamical matrix. For LiBC , the values are 750 cm^{-1} for a (8,8,4) reciprocal lattice division (30 \mathbf{k} -points in irreducible BZ (IBZ)) and 712 cm^{-1} for a (32,32,16) reciprocal lattice division (918 \mathbf{k} -points in IBZ). These frequency values from linear response calculation for MgB_2 are 585 cm^{-1} (BZ integrals done with (12,12,12) reciprocal lattice divisions) and 532 cm^{-1} (BZ integrals done with (24,24,24) reciprocal lattice divisions). The frequency values quoted in Ref. [166] are 58 meV (468 cm^{-1}) and 68 meV (548 cm^{-1}) for MgB_2 and LiBC , respectively. In addition to linear response, we have carried out frozen

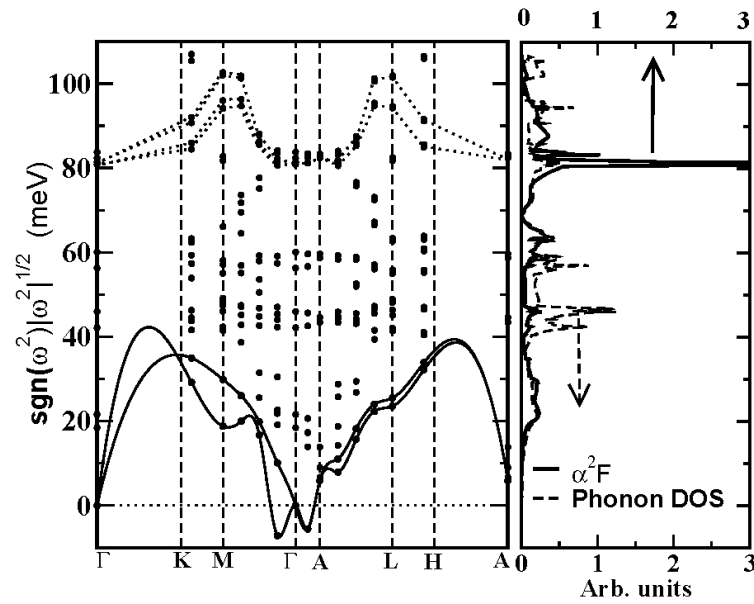


Figure 25. Phonon frequencies and DOS, and the Eliashberg spectral function for $\text{Li}_{0.5}\text{BeN}$. The frequencies for 30 wave vectors, generated by (8,8,4) reciprocal lattice divisions, were calculated. The BZ sums in calculating the dynamical matrix for the Γ point and the wave vector between Γ and A were carried out for a (32,32,16) mesh. For all other wave vectors, the mesh size for the dynamical matrix calculation was (8,8,4). The dotted lines show the softening of the E_{2g} phonon branch due to EP coupling. Solid lines are drawn to show unstable phonon modes for wave vectors along Γ -A and Γ -M directions.

phonon calculations using the full potential LAPW method to estimate these frequencies. The values are 800 cm^{-1} for LiBC and 536 cm^{-1} for MgB_2 . Using our calculated values of $N_\sigma(0)$, deformation potentials D , E_{2g} -mode frequencies, the required mass factors and the scaling relation of Eq.(23), we find λ to be 1.2 times larger for Li0.5BC compared with MgB_2 , i.e. $\lambda = 1.0$ for $\text{Li}_{0.5}\text{BC}$. Using $\omega_{ln} = \omega(E_{2g})$, $\mu^* = 0.1$, and $\lambda = 1.0$, we get $T_c \simeq 70 \text{ K}$. This value is close to the value $T_c = 65 \text{ K}$ obtained by Dewhurst *et al.* [172] using a pseudopotential-based method, and is 30 % less than the value quoted by Rosner *et al.* [166]. Scaling arguments based on Eq.(23), the calculated value of $\omega(E_{2g})$ and comparison with MgB_2 yield $\lambda = 0.6$ and $T_c = 21.0$ for $\text{Li}_{0.5}\text{BeN}$. These results are summarized in Table 8.

To date, attempts to de-intercalate Li from LiBC and/or observe the superconducting character of LiBC have failed [173]. As a corollary, there does not seem to be any point in trying to stabilize hexagonal LiBeN either. It is, however, important to understand where the faults in arguments lie. One could question the validity of the scaling arguments based on Eq.(23). Since only about half of the total EP coupling constant comes from the E_{2g} phonons, the scaling estimates based on the relative strengths of the E_{2g} -mode

coupling only are somewhat inadequate. A full linear response calculation of the EP coupling gives a lower value $\lambda = 0.76$. Using this value (0.76) of λ and the calculated value of ω_{in} in the McMillan equation results in a lower $T_c = 34$ K for $\mu^* = 0.1$. This result, obtained by using a uniform division of the BZ and a modest number of wave vectors (918 wave vectors in the IBZ) for the sums involved in the Hopfield matrix, may not be accurate. Since most of the contribution arises from the narrow cylindrical sheet of the Fermi surface centered about the Γ -point with its axis along the Γ -A direction, a uniform sampling of the hexagonal BZ may not accurately capture the full EP coupling, a point emphasized by several authors [132, 168]. However, this point does not seem relevant in understanding why experiments have failed entirely to detect superconductivity in hole-doped LiBC.

Several authors have maintained that the anharmonicity of the phonons, and particularly that of the Γ -point E_{2g} phonon, should play an important role in EP coupling [44, 134, 174] in MgB_2 and similar compounds. The anharmonicity of the E_{2g} mode is likely to reduce linear EP coupling [44]. However, it is also likely to introduce significant multi-phonon, i.e. nonlinear, EP coupling. According to Boeri *et al.* [174] the small value of the Fermi energy for the holes in the σ -band, with entire portions of the Fermi surface disappearing upon E_{2g} distortion, is the fundamental origin of anharmonicity. It is conceivable that this effect is more pronounced in hole-doped LiBC. Shukla *et al.* [175] have measured the phonon linewidth in a single crystal of MgB_2 using inelastic x-ray scattering. The measured intrinsic linewidth of the E_{2g} branch is strongly anisotropic in the BZ, and it is particularly large along the Γ -A direction, varying from 20 to 28 meV. Their density functional calculations reveal that most of the linewidth is due to linear EP coupling, with that due to anharmonicity being an order of magnitude smaller.

None of these issues, however, clearly indicate why hole-doped LiBC should be non-superconducting despite strong indications to the contrary based on linear EP calculations, which have been successful on numerous other occasions. An obvious concern, of course, is the stability of the compound itself at such high levels (25-50%) of hole-doping via removal of Li. Even if the compound stays stable and retains its structure, there may be substantial changes in the vibrational properties: changes in phonon frequencies, including appearance of localized phonons. The VCA approach clearly fails to capture any such change.

One key point, according to Pickett and co-workers [168], is that LiBC and, to some extent, MgB_2 represent cases of extreme EP coupling, where one or a few phonon modes couple extremely strongly to electrons, with the rest of the phonons showing only modest coupling. This anomalously large

coupling leads to strong Kohn anomalies (discontinuities in the derivatives of the phonon dispersion curves) and large softening of these modes. For hole-doped LiBC, this softening of the Γ -point E_{2g} phonon is clear in Fig. 24 and in Fig. 2 of Ref. [168] (ω^2 decreases by $\sim 60\%$). The phonon linewidths, ordinarily not more than 1% of the frequency, become comparable to the frequencies themselves. In MgB_2 , the linewidth for the E_{2g} branch can be as high as one third of the frequency [175], as revealed by both experiment and calculations. In Li_xBC , the E_{2g} linewidth is even higher, reaching as high as 50% of the frequency itself, rendering the concept of a 'phonon' rather ill-defined. Electrons in such systems can at best be described as polarons (or similar such entities). The polaronic effects should strongly renormalize the energy bands, to the extent that the adiabatic approximation, which forms the basis of the Migdal-Eliashberg theory, becomes invalid [176]. In principle, the use of a δ -function in Eq. (16) is no longer correct.

Pickett and co-workers [168], via approximate analytical treatment, considered the mode-specific EP coupling constant λ_Q and observed that for the E_{2g} modes these scale inversely with k_F^2 , k_F being the Fermi wave vector for the cylindrical Fermi surface related to the σ -band. For vanishing σ hole-doping, these coupling constants will diverge. Although they remain integrable (and total λ remains finite), the divergence of the mode-specific coupling constants does pose a serious challenge to their accurate numerical evaluation. Indeed, for MgB_2 the Γ point E_{2g} -mode coupling constant approaches 25, and in hole-doped LiBC it is even higher. One important point [168, 177] is that the two-dimensionality of the electron dispersion in these systems can cause large redistribution of the coupling strength with increasing doping level, without any direct effect on T_c itself. Once $N(0)$ is saturated, the increase in $2k_F$ with increasing hole-doping is accompanied by a reduction in λ_Q for a given Q/k_F , so that the integral over all Q for the total EP constant remains unchanged.

The success of the conventional Eliashberg theory in explaining superconductivity in MgB_2 appears to be fortunate in view of the above discussion. For systems like Li_xBC with stronger anomalous EP coupling, it seems that all aspects of the theory need to be revisited.

4. Conclusions

The examples discussed in the previous section show that *ab initio* density-functional calculations of the Eliashberg function and the electron-phonon coupling have successfully explained the observed superconducting properties of many well-known as well as recently discovered superconductors. In cases where the calculated results differ from the measured superconducting properties, calculations have at least provided guidance toward necessary future

work, both in terms of theory and experiment. The case of MgB_2 is an example of a notable success of the present state of *ab initio* calculations. However, there are issues related to the anharmonicity of the modes and multi-phonon coupling that are still in need of further study. MgB_2 is an example of a system where unusually large electron-phonon coupling along the $\Gamma-A$ phonon branch determines basically the complete electron-phonon coupling for the system. Anomalously large coupling for these modes also leads to large softening and linewidths, verified both experimentally and via calculations, with experiment and theory being in good agreement. Despite coupling primarily via a few phonon modes with large linewidth, the essential aspects of superconductivity in MgB_2 seems to be captured by the Migdal-Eliashberg theory. The anomalous EP coupling effects are even stronger in hole-doped LiBC, making the predictions of Migdal-Eliashberg theory in this case highly dubious. The example of LiBC serves to illustrate severe inadequacies in the state of our theoretical understanding of superconductivity in systems where only a few phonon modes couple extremely strongly to electrons, which results in phonon linewidths that are as large as the frequencies themselves. Indeed, for such systems the concept of a phonon, computation of electron energy bands, polaronic effects, nonadiabatic renormalization of phonons, and electron-phonon coupling all need to be re-examined.

Acknowledgments

SKB would like to acknowledge the financial support provided by the Natural Sciences and Engineering Research Council of Canada. JK would like to thank the German Science Foundation for financial support within the priority program DFG-SPP 1236 (KO1924/3-1). The generous hospitality of Prof. Ole K. Andersen at the Max-Planck-Institute of Solid State Research, Stuttgart, Germany, where a part of this work was carried out, is gratefully acknowledged.

Very special thanks from both authors are due to Igor Mazin and Ole K. Andersen for many stimulating discussions and their support in the past. Further, JK would like to acknowledge many enlightening discussions on superconductivity with Oleg Dolgov, Alexander A. Golubov and Reinhard K. Kremer. SKB is grateful to B. Mitrović for valuable discussions and guidance with the literature.

References

1. Grimvall, G., 1981, *The Electron-Phonon Interaction in Metals* (North-Holland, Amsterdam).
2. Parks, R. D., 1969, *Superconductivity, Vols. 1 and 2* (Marcel Dekker Inc. New York).
3. Bardeen, J., Cooper, L. N., and Schrieffer, J. R., 1957, *Phys. Rev.* **108**, 1175.

4. Rickayzen, G., 1965, *Theory of Superconductivity* (Wiley (Interscience), New York).
5. de Gennes, P. G., 1966, *Superconductivity in Metals and Alloys* (Benjamin, New York).
6. Tinkham, M., 1975, *Introduction to Superconductivity* (McGraw-Hill, New York).
7. Dolgov, O. V., and Maksimov, E. G., 1982, *Sov. Phys. Usp.* **25**, 688.
8. Allen, P. B., and Mitrovic, B., 1982, *Theory of superconducting T_c* (New York: Academic Press), volume 37, p. 1.
9. Carbotte, J. P., 1990, *Rev. Mod. Phys.* **62**, 1027.
10. Marsiglio, F., and Carbotte, J. P., 2001, cond-mat/0106143 v1 .
11. Savrasov, S. Y., Savrasov, D. Y., and Andersen, O. K., 1994, *Phys. Rev. Lett.* **72**, 372.
12. Savrasov, S. Y., 1996, *Phys. Rev. B* **54**, 16470.
13. Savrasov, S. Y., and Savrasov, D. Y., 1996, *Phys. Rev. B* **54**, 16487.
14. Onnes, H. K., Investigations into the properties of substances at low temperatures, which have led, amongst other things, to the preparation of liquid helium, URL http://nobelprize.org/nobel_prizes/physics/laureates/1913/onn%es-lecture.pdf.
15. Meißner, W., and Ochsenfeld, R., 1933, *Naturwissenschaften* **21**, 787.
16. Abrikosov, A. A., 1952, *Doklady Akademii Nauk SSSR* **86**, 489.
17. Josephson, B. D., 1962, *Phys. Lett.* **1**, 251.
18. Ginzburg, V. L., and Landau, L. D., 1950, *Zh. Eksp. Theor. Fiz.* **20**, 1064.
19. Frölich, H., 1950, *Phys. Rev.* **79**, 845.
20. Maxwell, E., 1950, *Phys. Rev.* **78**, 477.
21. Reynolds, C., Serin, B., Wright, W., and Nesbit, L., 1950, *Phys. Rev.* **78**, 487.
22. Bardeen, J., 1950, *Phys. Rev.* **79**, 167.
23. Bardeen, J., and Pines, D., 1955, *Phys. Rev.* **99**, 1140.
24. Cooper, L., 1956, *Phys. Rev.* **104**, 1189.
25. Bardeen, J., Cooper, L. N., and Schrieffer, J. R., 1957, *Phys. Rev.* **108**, 162.
26. Bednorz, J. G., and Müller, K. A., 1986, *Z. Phys. B* **64**, 189.
27. Scalapino, D., 1969 (Marcel Dekker Inc. New York), volume 1.
28. Mitrović, B., 1979, *M.Sc. Thesis* (McMaster University, Canada).
29. Migdal, A. B., 1958, *Zh. Eksp. Theor. Fiz.* **34**, 1438.
30. Migdal, A. B., 1958, *Sov. Phys. JETP* **7**, 996.
31. Eliashberg, G. M., 1960, *Zh. Eksp. Theor. Fiz.* **38**, 966.
32. Eliashberg, G. M., 1960, *Sov. Phys. JETP* **11**, 696.
33. Eliashberg, G. M., 1960, *Zh. Eksp. Theor. Fiz.* **39**, 1437.
34. Gorkov, L., 1958, *Sov. Phys. JETP* **7**, 505.
35. Morel, P., and Anderson, P., 1962, *Phys. Rev.* **125**, 1263.
36. Scalapino, D., Schrieffer, J., and Wilkins, J., 1966, *Phys. Rev.* **148**, 263.
37. Mahan, G., 1981 (New York: Plenum Press), chapter 3, pp. 123–222.
38. Hohenberg, P., and Kohn, W., 1964, *Phys. Rev.* **136**, B864.
39. Kohn, W., and Sham, L. J., 1965, *Phys. Rev.* **140**, A1133.
40. Jones, R. O., and Gunnarsson, O., 1989, *Rev. Mod. Phys.* **61**, 689.
41. Baroni, S., de Gironcoli, S., Dal Corso, A., and Giannozzi, P., 2001, *Rev. Mod. Phys.* **73**, 515.
42. Nagamatsu, J., Nakagawa, N., Muranaka, T., Zenitani, Y., and Akimitsu, J., 2001, *Nature (London)* **410**, 63.
43. Kortus, J., Mazin, I. I., Belashchenko, K. D., Antropov, V. P., and Boyer, L. L., 2001, *Phys. Rev. Lett.* **86**, 4656.

44. Liu, A. Y., Mazin, I. I., and Kortus, J., 2001, Phys. Rev. Lett. **87**, 087005.
45. Allen, P. B., 1971, Phys. Rev. B **3**, 305.
46. Lüders, M., Marques, M. A. L., Lathiotakis, N. N., Floris, A., Profeta, G., Fast, L., Continenza, A., Massidda, S., and Gross, E. K. U., 2005, Phys. Rev. B **72**, 024545.
47. Marques, M. A. L., Lüders, M., Lathiotakis, N. N., Profeta, G., Floris, A., Fast, L., Continenza, A., Gross, E. K. U., and Massidda, S., 2005, Phys. Rev. B **72**, 024546.
48. B. Mitrović, private communications.
49. Allen, P. B., and Dynes, R. C., 1975, Phys. Rev. B **12**, 905.
50. McMillan, W. L., 1968, Phys. Rev. **167**, 331.
51. Dynes, R., 1972, Sol. St. Comm. **10**, 615.
52. Allen, P., and Dynes, R., 1975, J. Phys. C: Solid St. Phys. **8**, L158.
53. Schrieffer, J., Scalapino, D., and Wilkins, J., 1963, Phys. Rev. Lett. **10**, 336.
54. Rowell, J., Anderson, P., and Thomas, D., 1963, Phys. Rev. Lett. **10**, 334.
55. McMillan, W., and Rowell, J., 1965, Phys. Rev. Lett. **14**, 108.
56. McMillan, W. L., and Rowell, J.M., 1969 (Marcel Dekker Inc. New York), volume 1.
57. See Bell Telephone Laboratories internal report by J.M. Rowell, W.L. McMillan and R. C. Dynes; and Technical Report 7 by P.B. Allen, TCM Group, Cavendish Laboratory, Madingley Road, Cambridge CB3 0HE, U.K.
58. Galkin, A., D'yachenko, A., and Svistunov, V., 1974, JETP **39**, 1115.
59. Svistunov, V., D'yachenko, A., and Belogolovskii, M. A., 1978, J. Low Temp. Phys. **31**, 339.
60. Wolf, E. L., 1985, *Principles of Electron Tunneling Spectroscopy* (Oxford University Press London).
61. Gonnelli, R. S., Ummarino, G. A., and Stepanov, V. A., 1997, Physica C **275**, 162.
62. Dolgov, O. V., Gonnelli, R. S., Ummarino, G. A., Golubov, A. A., Shulga, S. V., and Kortus, J., 2003, Phys. Rev. B **68**, 132503.
63. Devreese, J., Doren, V. V., and Camp, P. V., 1983, *Ab Initio Calculation of Phonon Spectra* (Plenum, N.Y.).
64. Devreese, J., and Camp, P. V., 1985, *Electronic Structure, Dynamics, and Quantum Structural Properties of Condensed Matter* (Plenum, N.Y.).
65. Heine, V., and Weaire, D., 1970, Solid State Physics **24**, 366.
66. Chadi, D., and Martin, R., 1976, Solid State Communications **19**, 643.
67. Baroni, S., Giannozzi, P., and Testa, A., 1987, Phys. Rev. Lett. **58**, 1861.
68. Gaspary, G., and Gyorfy, B., 1972, Phys. Rev. Lett. **28**, 801.
69. Dacorogna, M., Cohen, M., and Lam, P., 1985, Phys. Rev. Lett. **55**, 837.
70. Dacorogna, M., Chang, K., and Cohen, M., 1985, Phys. Rev. B **32**, 1858.
71. Lam, P., Dacorogna, M., and Cohen, M., 1986, Phys. Rev. B **34**, 5065.
72. Chang, K., and Cohen, M., 1986, Phys. Rev. B **34**, 4552.
73. Liu, A., Chang, K., and Cohen, M., 1988, Phys. Rev. B **37**, 6344.
74. Weber, W., 1987, Phys. Rev. Lett. **58**, 1371.
75. Weber, W., 1984, Physica **126B**, 217.
76. Weber, W., 1984 (Plenum, N.Y.), volume 113, pp. 345–462.
77. Rudin, S., Liu, A., Freericks, J., and Quandt, A., 2001, Phys. Rev. B **63**, 224107.
78. Calandra, M., and Mauri, F., 2005, Phys. Rev. Lett. **95**, 237002.
79. Kim, J., Boeri, L., Kremer, R., and Razavi, F., 2006, Phys. Rev. Lett. **96**, 217002.

80. Hybersten, M., and Louie, S., 1987, Phys. Rev. B **35**, 5585.
81. Lee, K.-H., Chang, K., and Cohen, M., 1995, Phys. Rev. B **52**, 1425.
82. Lee, K.-H., and Chang, K., 1996, Phys. Rev. B **54**, 1419.
83. Moon, C.-Y., Kim, Y.-H., and Chang, K., 2004, Phys. Rev. B **70**, 104522.
84. Andersen, O. K., 1975, Phys. Rev. B **12**, 3060.
85. Andersen, O. K., and Jepsen, O., 1984, Phys. Rev. Lett. **53**, 2571.
86. Skriver, H. L., 1984, *The LMTO Method, Muffin-Tin Orbitals and Electronic Structure* (Springer, Berlin).
87. Sternheimer, R. M., 1954, Phys. Rev. **96**, 951.
88. Sternheimer, R. M., 1957, Phys. Rev. **107**, 1565.
89. Sternheimer, R. M., 1959, Phys. Rev. **115**, 1198.
90. Pulay, P., 1969, Mol. Phys. **17**, 197.
91. Blöchl, P. E., Jepsen, O., and Andersen, O. K., 1994, Phys. Rev. B **49**(23), 16223.
92. Allen, P. B., 1972, Phys. Rev. B **6**(7), 2577.
93. Savrasov, S. Y., and Andersen, O. K., 1996, Phys. Rev. Lett. **77**, 4430.
94. Janak, J. F., Moruzzi, V. L., and Williams, A. R., 1975, Phys. Rev. B **12**, 1257.
95. Hedin, L., and Lundqvist, B. I., 1971, J. Phys. C **4**, 2064.
96. Bose, S. K., Kato, T., and Jepsen, O., 2005, Phys. Rev. B **72**, 184509.
97. Bose, S. K., unpublished calculations.
98. Keller, T., Aynajian, P., Habicht, K., Boeri, L., Bose, S. K., and Kemier, B., 2006, Phys. Rev. Lett. **96**, 225501.
99. Schilling, J. S., 2006 (Springer-Verlag, Hamburg), see also condmat/0604090.
100. Rajagopalan, M., Alouani, M., and Christensen, N. E., 1989, J. Low Temp. Phys. **75**, 1.
101. Tissen, V. G., Ponyatovski, E. G., and Nefedova, M. V., 1996, Phys. Rev. B **53**, 8238.
102. Pickett, W. E., Freeman, A. J., and Koelling, D. D., 1980, Phys. Rev. B **22**, 2695.
103. Wühl, H., Eichler, A., and Wittig, J., 1973, Phys. Rev. Lett. **31**, 1393.
104. Hamed, F., Razavi, F. S., Zaleski, H., and Bose, S. K., 1991, Phys. Rev. B **43**, 3649.
105. Bose, S. K., Kudrnovský, J., Razavi, F. S., and Andersen, O. K., 1991, Phys. Rev. B **43**, 110.
106. McMahon, M., and Nelves, R., 1993, Phys. Rev. B **47**, 8337.
107. Chang, K., Dacorogna, M., Cohen, M., Mignot, J., Chouteau, G., and Martinez, G., 1985, Phys. Rev. Lett. **54**, 2375.
108. Hamlin, J. J., Tissen, V. G., and Schilling, J. S., 2006, Phys. Rev. B **73**, 094522.
109. Yin, Z. P., Savrasov, S. Y., and Pickett, W. E., 2006, Phys. Rev. B **74**, 094519.
110. Deemyad, S., and Schilling, J. S., 2003, Phys. Rev. Lett. **91**, 167001.
111. Struzhkin, V. V., Eremets, M. I., Gan, W., Mao, H. K., and Hemley, R. J., 2002, Science **298**, 1213.
112. Shimizu, K., Kimura, H., Takao, D., and Amaya, K., 2002, Nature **419**, 597.
113. See W. E. Pickett, cond-mat/0603428.
114. Shimizu, K., Kimura, T., Furomoto, S., Takeda, K., Kotani, K., Onuki, Y., and Amaya, K., 2001, Nature (London) **412**, 316.
115. Saxena, S., and Littlewood, P., 2001, Nature (London) **412**, 290.
116. Jaccard, D., Holmes, A., Behr, G., Inada, Y., and Onuki, Y., 2002, Phys. Lett. A **299**, 282.

117. Mazin, I. I., Papaconstantopoulos, D. A., and Mehl, M. J., 2002, Phys. Rev. B **65**, 100511(R).
118. Bose, S. K., Dolgov, O. V., Kortus, J., Jepsen, O., and Andersen, O. K., 2003, Phys. Rev. B **67**, 214518.
119. Söderland, P., Moriarty, J., and Mills, J. M., 1996, Phys. Rev. B **53**, 14063.
120. Alfé, D., Price, G. D., and Gillan, M. J., 2001, Phys. Rev. B **64**, 045123.
121. Perdew, J. P., Chevary, J. A., Vosko, S. H., Jackson, K. A., Pederson, M. R., Singh, D., and Fiolhais, C., 1992, Phys. Rev. B **45**, 6671.
122. Merkel, S., Goncharov, A. F., Mao, H., Gillet, P., and Hemley, R. J., 2000, Science **288**, 1626.
123. Goncharov, A. F., Gregoryanz, E., Struzhkin, V. V., Hemley, R. J., Mao, H., Boctor, N., and Huang, E., 2001, cond-mat **0112404**.
124. Steinle-Neumann, G., Stixrude, L., Cohen, R. E., and Kiefer, B., 2001, cond-mat **0111487**.
125. Steinle-Neumann, G., Stixrude, L., and Cohen, R. E., 1999, Phys. Rev. B **60**, 791.
126. Mailhot, C., Grant, J. B., and McMahan, A., 1990, Phys. Rev. B **42**, 9033.
127. Eremets, M. I., Struzhkin, V. V., Mao, H., and Hemley, R. J., 2001, Science **293**, 272.
128. Ma, Y., Tse, J. S., Klug, D. D., and Ahuja, R., 2004, Phys. Rev. B **70**, 214107.
129. Segall, D. E., and Arias, T. A., 2003, Phys. Rev. B **67**, 064105.
130. Giannozzi, P., de Gironcoli, S., Pavone, P., and Baroni, S., 1991, Phys. Rev. B **43**, 7231.
131. An, J. M., and Pickett, W. E., 2001, Phys. Rev. Lett. **86**, 4366.
132. Kong, Y., Dolgov, O. V., Jepsen, O., and Andersen, O. K., 2001, Phys. Rev. B **64**(2), 020501.
133. Bohnen, K.-P., Heid, R., and Renker, B., 2001, Phys. Rev. Lett. **86**(25), 5771.
134. Kunc, K., Loa, I., Syassen, K., Kremer, R. K., and Ahn, K., 2001, J. Phys: Condens. Matter **13**, 9945.
135. Choi, H. J., Roundy, D., Sun, H., Cohen, M. L., and Louie, S. G., 2002, Phys. Rev. B **66**, 020513.
136. Choi, H. J., Roundy, D., Sun, H., Cohen, M. L., and Louie, S. G., 2002, Nature (London) **418**, 758.
137. Canfield, P. C., and G. W. Crabtree, G. W., 2003, Physics Today **56**(3), 34.
138. Shulga, S. V., Drechsler, S.-L., Eschrig, H., Rosner, H., and Pickett, W. E., 2001, cond-mat/0103154. Please note, that these authors suggested two-band superconductivity in MgB₂ earlier than most other authors. Unfortunately, this suggestion was based on the assumption that in addition to electron-phonon coupling there is another coupling to an unknown low energy boson mode.
139. Crabtree, G., Kwok, W., Canfield, P. C., and Bud'ko, S. L., 2003, Physica C **385**, 1, special issue on MgB₂.
140. Golubov, A. A., Kortus, J., Dolgov, O. V., Jepsen, O., Kong, Y., Andersen, O. K., Gibson, B. J., Ahn, K., and Kremer, R. K., 2002, J. Phys: Condens. Matter **14**, 1353.
141. Brinkman, A., Golubov, A. A., Rogalla, H., Dolgov, O. V., Kortus, J., Kong, Y., Jepsen, O., and Andersen, O. K., 2002, Phys. Rev. B **65**(18), 180517.
142. Golubov, A. A., Brinkman, A., Dolgov, O. V., Kortus, J., and Jepsen, O., 2002, Phys. Rev. B **66**(5), 054524.

143. Dolgov, O. V., Kremer, R. K., Kortus, J., Golubov, A. A., and Shulga, S. V., 2005, *Phys. Rev. B* **72**(2), 024504.
144. Mazin, I. I., Andersen, O. K., Jepsen, O., Dolgov, O. V., Kortus, J., Golubov, A., Kuz'menko, A. B., and van der Marel, D., 2002, *Phys. Rev. Lett.* **89**(10), 107002.
145. Golubov, A. A., and Mazin, I. I., 1997, *Phys. Rev. B* **55**(22), 15146.
146. Mazin, I. I., Andersen, O. K., Jepsen, O., Golubov, A. A., Dolgov, O. V., and Kortus, J., 2004, *Phys. Rev. B* **69**(5), 056501.
147. Mitrović, B., 2004, *J. Phys.: Condens. Matter* **16**, 9013.
148. Erwin, S. C., and Mazin, I. I., 2003, *Phys. Rev. B* **68**(13), 132505.
149. Kortus, J., Dolgov, O. V., Kremer, R. K., and Golubov, A. A., 2005, *Phys. Rev. Lett.* **94**, 027002.
150. **Kortus, J., 2007, *Physica C* . Incomplete**
151. Khan, F. S., and Allen, P. B., 1984, *Phys. Rev. B* **29**, 3341.
152. Ekimov, E. A., Sidorov, V. A., Bauer, E. D., Melnik, N. N., Curro, N. J., Thompson, J. D., and Stishov, S. M., 2004, *Nature (London)* **428**, 542.
153. Zhang, R. J., Lee, S. T., and Lam, Y. W., 1996, *Diamond Rel. Mater.* **5**, 1288.
154. Boeri, L., Kortus, J., and Andersen, O., 2006, *J. Phys. Chem. Solids* **67**, 552.
155. Boeri, L., Kortus, J., and Andersen, O. K., 2004, *Phys. Rev. Lett.* **93**(23), 237002.
156. Ortolani, M., Lupi, S., Baldassarre, L., Schade, U., Calvani, P., Takano, Y., Nagao, M., Takenouchi, T., and Kawarada, H., 2006, *Phys. Rev. Lett.* **97**(9), 097002.
157. Xiang, H. J., Li, Z., Yang, J., Hou, J. G., and Zhu, Q., 2004, *Physical Review B (Condensed Matter and Materials Physics)* **70**(21), 212504 (pages 4), URL <http://link.aps.org/abstract/PRB/v70/e212504>.
158. Medvedeva, N. I., Ivanovskii, A. L., Medvedeva, J. E., and Freeman, A. J., 2001, *Phys. Rev. B* **64**, 020502(R).
159. Singh, P., 2001, *Phys. Rev. Lett.* **87**, 087004.
160. Mehl, M. J., Papaconstantopoulos, D. A., and Singh, D. J., 2001, *Phys. Rev. B* **64**, 140509(R).
161. Belaschenko, K. D., van Schilfgaarde, M., and Antropov, V. P., 2001, *Phys. Rev. B* **64**, 092503.
162. Ravindran, P., Vajeeston, P., Vidya, R., Kjekshus, A., and Fjellvg, H., 2001, *Phys. Rev. B* **64**, 224509.
163. Lipp, A., and Roder, M., 1966, *Z. Anorg. Chem.* **334**, 225.
164. Profeta, G., Continenza, A., Bernardini, F., and Massidda, S., 2001, *Phys. Rev. B* **65**, 054502.
165. See e.g. Inorganic Crystal Structure Database, <http://icsd/dif/icsd>.
166. Rosner, H., Kitaigorodsky, A., and Pickett, W., 2002, *Phys. Rev. Lett* **88**, 127001.
167. Although $\omega(E_{2g})$ was positive for this lattice parameter, imaginary value for two of the E_{1u} modes indicated possible structural instability at this volume.
168. An, J. M., Savrasov, S. Y., Rosner, H., and Pickett, W. E., 2002, *Phys. Rev. B* **66**, 220502.
169. Wörle, M., Nesper, R., Mair, G., Schwarz, M., and Schnering, H. V., 1995, *Z. Anorg. Chem.* **621**, 1153.
170. Somer, M. *et al.*, 1996, *Z. Kristallogr.* **211**, 635.

-
171. Pronin, A. V., Pucher, K., Lunkenheimer, P., Krimmel, A., and Loidl, A., 2003, *Phys. Rev. B* **67**, 132502.
 172. Dewhurst, J. K., Sharma, S., Ambrosch-Draxl, C., and Johansson, B., 2003, *Phys. Rev. B* **68**, 20504.
 173. See references in W.E. Pickett, cond-mat/0603428.
 174. Boeri, L., Bachelet, G. B., Cappelluti, E., and Pietronero, L., 2002, *Phys. Rev. B* **65**, 214501.
 175. Shukla, A., Calandra, M., d'Astuto, M., Lazzeri, M., Mauri, F., and Bellin, C., 2003, *Phys. Rev. Lett.* **90**, 095506.
 176. Alexandrov, A., and Capellmann, H., 1991, *Phys. Rev. B* **43**, 2042.
 177. O.K. Andersen, private communications.